Computer Methods in Applied Mechanics and Engineering 448 (2026) 118432

Contents lists available at ScienceDirect

Comput. Methods Appl. Mech. Engrg.

journal homepage: www.elsevier.com/locate/cma

Second order three-dimensional serendipity virtual elements for hyperelasticity: Static and dynamic analysis

Bing-Bing Xu [a,*], Lourenco Beirao da Veiga [b], Yongjie Jessica Zhang [c], Peter Wriggers [a]

[a] Institute of Continuum Mechanics, Leibniz University Hannover, Hannover, Germany
[b] University of Milan-Bicocca, Milano, Italy
[c] Department of Mechanical Engineering, Carnegie Mellon University, Pittsburgh, Pennsylvania, USA

ARTICLE INFO

Keywords:
Virtual element method
Hyperelasticity
Dynamic analysis

ABSTRACT

In this work, a three-dimensional (3D) second-order serendipity virtual element method (S-VEM) is developed for the static and dynamic analysis of hyperelastic materials. The VEM framework is based on the projection of unknown basis functions onto polynomial spaces, allowing for flexible discretization with arbitrary polyhedral meshes. While most existing VEM formulations for 3D mechanical problems are discretized using first-order formulations, higher-order schemes offer improved precision, especially for nonlinear problems. However, conventional second-order VEM formulations introduce additional degrees of freedom (DOFs), such as body and surface moments, which complicate the implementation and reduce computation efficiency. To address this challenge, we propose a novel 3D second-order serendipity VEM that avoids any extra moment-related DOFs. This is the first application of a serendipity VEM to 3D static and dynamic problems in hyperelasticity. Furthermore, by integrating advanced mesh generation techniques, the proposed method enables hybrid simulations that combine second-order serendipity VEM and FEM to efficiently handle complex geometries.

1. Introduction

Hyperelastic materials, which exhibit nonlinear elastic behavior under finite deformations, are widely used in engineering and biomedical applications, such as soft robotics, elastomers, and biological tissues. Accurate simulation of the mechanical behavior under large strains is essential in the design and analysis of hyperelastic materials. Basically, there are two types of hyperelastic problems we considered: quasi-static problems and dynamic problems. Compared to the quasi-static problems, dynamic hyperelasticity further considers inertial effects, enabling the prediction of time-dependent responses.

Over the past decades, various numerical techniques have been developed for the hyperelasticity. Among them, the finite element method (FEM) has been the most widely used approach for both quasi-static and dynamic problems involving hyperelastic materials [1–3]. However, FEM often suffers from mesh distortion when dealing with large deformations, leading to reduced accuracy or numerical instability. Meshless methods, such as the smoothed particle hydrodynamics (SPH) [4–6] has been proposed to overcome this limitation. Nevertheless, SPH methods also exhibit their own forms of numerical instability. In addition, other advanced

* Corresponding author.
E-mail address: bingbing.xu@ikm.uni-hannover.de (B.-B. Xu).

https://doi.org/10.1016/j.cma.2025.118432
Received 17 June 2025; Received in revised form 24 August 2025; Accepted 20 September 2025
Available online 29 September 2025

discretization techniques such as isogeometric analysis (IGA) [7] have been explored to improve robustness and accuracy in the simulation of hyperelastic materials.

The virtual element method (VEM) [8,9] is a modern generalization of the FEM that enables the use of arbitrary polygonal and polyhedral meshes while offering excellent numerical stability. Different from the traditional polygonal FEM, VEM uses a projection operator from the virtual element space to a polynomial space to define the basis functions. This projection is fully defined by the degrees of freedom located on the element boundaries, allowing for great flexibility in mesh design and element shape. The VEM has been successfully applied to various engineering problems, such as hyperelastic materials at finite deformations [10–13], contact problems [14–17], phase field fractural mechanics [18–20], and finite elastoplastic deformations [21–23]. In addition, the VEM has been extended to the elastodynamics problems [24–27]. A review of VEM and associated code can be found in the references [28–30].

So far, most of the three-dimensional VEMs for nonlinear problems are based on the first-order anstaz functions ($k = 1$). However, the first-order VEM has some limitations in terms of accuracy and convergence rate, especially for incompressible problems or shear and bending-dominated problems [23]. Second-order formulations can significantly improve the accuracy and convergence of VEM, especially for problems with incompressible materials or bending-dominated problems. Limiting the discussion to H^1-conforming elliptic problems, up to now, high-order three-dimensionalVEMs have been proposed with a high-order polynomial degree (up to $k = 10$) [31–33] for the Poisson equation. But there are only a few second-order three-dimensional virtual element formulations for linear elastic problems and hyperelastic problems, see [34,35].

Within second-order VEM, the face moments and volume moments are introduced as additional degrees of freedoms for the calculation of the projection operator. As a result, the number of degrees of freedom increases significantly compared to the first-order VEM, leading to higher computational cost and implementation complexity. In this work, serendipity elements [36–38] will be constructed which delete the moment degrees of freedom on the surface and in the body, thereby reducing the degrees of freedom. Then the serendipity VEM (S-VEM) will be applied to the three-dimensional hyperelasticity problems. To the best of our knowledge, this work presents the first application of a three-dimensional S-VEM to nonlinear elastic problems, including both quasi-static and dynamic analyses of hyperelastic materials.

Due to its compatibility with arbitrary polygonal and polyhedral elements, the VEM is particularly well-suited for simulations involving complex geometries. The grid-based trimmed hexahedral (TH) meshing algorithm is a powerful tool for generating polyhedral and hexahedral-dominant meshes in such cases. For this hexahedron-polyhedron hybrid grid, hybrid VEM-FEM formulation can be employed to improve the accuracy and efficiency of complex geometric structures. In three-dimensional settings, the elimination of face moments enables the second-order serendipity VEM to be coupled with the second-order serendipity FEM (Q20).

The paper is organized as follows. Section 2 introduces the governing equations of hyperelasticity, including the balance laws, constitutive models, and the variational formulation. Section 3 provides a brief overview of the classical second-order VEM. The construction of the S-VEM is presented in Section 4. In Section 5, the discrete bilinear form of the S-VEM is derived for quasi-static hyperelastic problems. Section 6 extends the formulation to dynamic hyperelasticity, detailing the discretization of the dynamic equilibrium equations and the adopted time integration scheme. Then some mesh generation techniques and VEM-FEM hybrid format will be introduced in Section 7. Numerical examples, including both quasi-static and dynamic simulations, are provided in Section 8 to demonstrate the performance of the proposed method. Finally, conclusions and potential future directions are discussed in Section 9.

2. Equations of elastic mechanics

2.1. Governing equations

Hyperelastic materials are a type of material that exhibits nonlinear elastic behavior under finite deformation. As shown in Fig. 1, we assume the existence of a function $\boldsymbol{\varphi}$ which characterizes the motion of a body from the reference configuration Ω_0 to the current configuration Ω_t, we have

$$\boldsymbol{\varphi} : \Omega_0 \to \Omega_t, \quad \boldsymbol{X} \mapsto \boldsymbol{x} = \boldsymbol{\varphi}(\boldsymbol{X}), \quad \forall X \in \Omega_0, t \geq 0, \tag{1}$$

where $\boldsymbol{x}$ is the current position and $\boldsymbol{X}$ is the reference position of a material point. The displacement field $\boldsymbol{u}$ can be defined as $\boldsymbol{u} = \boldsymbol{x} - \boldsymbol{X}$. The deformation of a body can be described by the deformation gradient $\boldsymbol{F}$ as

$$\boldsymbol{F} = \frac{\partial \boldsymbol{x}}{\partial \boldsymbol{X}}. \tag{2}$$

As a strain measure, the Green-Lagrange strain tensor $\boldsymbol{E}$ is used

$$\boldsymbol{E} = \frac{1}{2}(\boldsymbol{C} - \boldsymbol{I}), \tag{3}$$

where $\boldsymbol{I}$ is the second order identity tensor. Here, the right Cauchy-Green deformation tensor $\boldsymbol{C}$ is defined as

$$\boldsymbol{C} = \boldsymbol{F}^T \cdot \boldsymbol{F}. \tag{4}$$

In the static equilibrium state, the balance of linear momentum can be expressed as

$$\nabla \cdot \boldsymbol{P} + \bar{\boldsymbol{f}} = \boldsymbol{0}, \tag{5}$$

where $\boldsymbol{P}$ is the first Piola-Kirchhoff stress tensor, and $\bar{\boldsymbol{f}}$ is the body force per unit volume. The Dirichlet and Neumann boundary conditions are given as

$$\boldsymbol{u} = \boldsymbol{u}_0, \quad \boldsymbol{x} \in \Gamma_D, \tag{6}$$

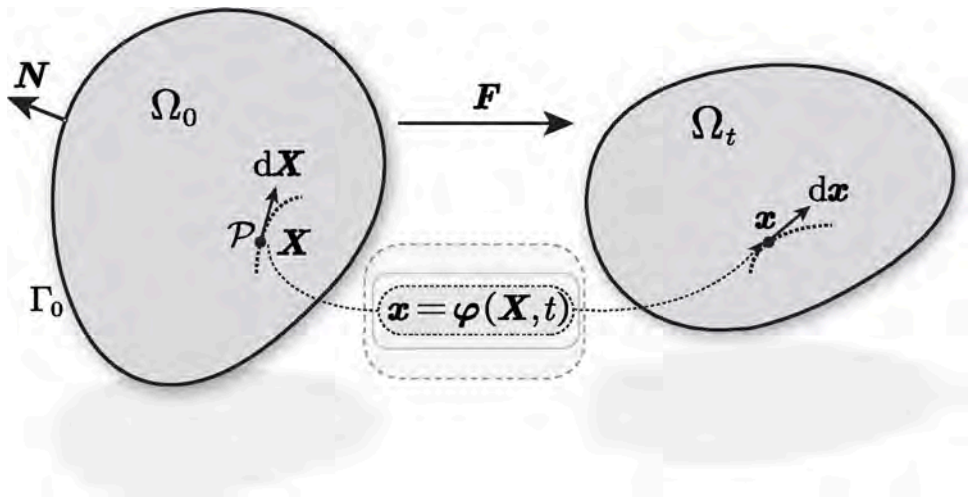

Fig. 1. Deformation of a body in the reference configuration and the current configuration.

$$\boldsymbol{P} \cdot \boldsymbol{N} = \bar{\boldsymbol{t}}, \quad \boldsymbol{x} \in \Gamma_N, \tag{7}$$

where $\boldsymbol{u}_0$ is the prescribed displacement, $\bar{\boldsymbol{t}}$ is the prescribed traction, Γ_D and Γ_N are the Dirichlet and the Neumann boundary, respectively.

2.2. Constitutive model

The mechanical behavior of hyperelastic materials is described by the strain energy density $\Psi(\boldsymbol{C})$. In this work, a compressible Non-Hookean material is selected

$$\Psi = \frac{\mu}{2}(I_1 - 3) - \mu \ln J + \frac{\lambda}{2}(\ln J)^2, \tag{8}$$

where μ and λ are the Lamé constants, $I_1 = \mathrm{tr}(\boldsymbol{C})$, and J is the determinant of the deformation gradient $\boldsymbol{F}$.

The second Piola-Kirchhoff stress tensor $\boldsymbol{S}$ for the Non-Hookean material follows as

$$\begin{aligned} \boldsymbol{S} &= 2\frac{\partial \Psi}{\partial \boldsymbol{C}} = \mu \boldsymbol{I} - 2\mu \frac{1}{J}\frac{\partial J}{\partial \boldsymbol{C}} + 2\lambda(\ln J)\frac{1}{J}\frac{\partial J}{\partial \boldsymbol{C}} \\ &= \mu\left(\boldsymbol{I} - \boldsymbol{C}^{-1}\right) + \lambda(\ln J)\boldsymbol{C}^{-1}. \end{aligned} \tag{9}$$

Lastly, the constitutive tensor $\boldsymbol{\mathcal{D}}$ is obtained as

$$\boldsymbol{\mathcal{D}} = 2\frac{\partial \boldsymbol{S}}{\partial \boldsymbol{C}} = \lambda \boldsymbol{C}^{-1} \otimes \boldsymbol{C}^{-1} + 2(\mu - \lambda \ln J)\boldsymbol{\mathcal{L}}, \tag{10}$$

where we can write in index notation as

$$\mathcal{L}_{IJKL} = -\frac{\partial \left(\boldsymbol{C}^{-1}\right)_{IJ}}{\partial C_{KL}} = \frac{1}{2}\left[\left(\boldsymbol{C}^{-1}\right)_{IK}\left(\boldsymbol{C}^{-1}\right)_{JL} + \left(\boldsymbol{C}^{-1}\right)_{IL}\left(\boldsymbol{C}^{-1}\right)_{JK}\right]. \tag{11}$$

For other compressible strain energy density functions, the corresponding second Piola-Kirchhoff stress and consistent constitutive tensor can be derived similarly. In practice, the use of automatic differentiation techniques can greatly simplify the derivation and implementation of these expressions, see e.g. [39].

2.3. Variational formulation

The potential energy of a solid can be written as

$$U(\boldsymbol{u}) = \int_\Omega \left[\Psi(\boldsymbol{u}) - \bar{\boldsymbol{f}} \cdot \boldsymbol{u}\right] \mathrm{d}\Omega_0 - \int_{\Gamma_N} \bar{\boldsymbol{t}} \cdot \boldsymbol{u} \, \mathrm{d}\Gamma_0. \tag{12}$$

The variational derivation yields the weak form of equilibrium equation

$$\delta U(\boldsymbol{u}) = \int_\Omega \left[\frac{\partial \Psi(\boldsymbol{u})}{\partial \boldsymbol{F}} : \delta \boldsymbol{F} - \bar{\boldsymbol{f}} \cdot \delta \boldsymbol{u}\right] \mathrm{d}\Omega_0 - \int_{\Gamma_N} \bar{\boldsymbol{t}} \cdot \delta \boldsymbol{u} \, \mathrm{d}\Gamma_0 = 0. \tag{13}$$

Considering the second Piola-Kirchhoff stress tensor $\boldsymbol{S} = \boldsymbol{F}^{-1} \cdot \boldsymbol{P}$, the weak form of equilibrium equation can be written as

$$\delta U(\boldsymbol{u}) = \int_\Omega \left[\boldsymbol{S} : \delta \boldsymbol{E} - \bar{\boldsymbol{f}} \cdot \delta \boldsymbol{u}\right] \mathrm{d}\Omega_0 - \int_{\Gamma_N} \bar{\boldsymbol{t}} \cdot \delta \boldsymbol{u} \, \mathrm{d}\Gamma_0 = 0. \tag{14}$$

Lastly, the weak form can be written as

$$a(\boldsymbol{u}, \delta\boldsymbol{u}) = \boldsymbol{f}(\delta\boldsymbol{u}), \tag{15}$$

with

$$a(\boldsymbol{u}, \delta\boldsymbol{u}) = \int_{\Omega} \boldsymbol{S} : \delta\boldsymbol{E}\, \mathrm{d}\Omega_0, \tag{16}$$

$$\boldsymbol{f}(\delta\boldsymbol{u}) = \int_{\Omega} \bar{\boldsymbol{f}} \cdot \delta\boldsymbol{u}\, \mathrm{d}\Omega_0 + \int_{\Gamma_N} \bar{\boldsymbol{t}} \cdot \delta\boldsymbol{u}\, \mathrm{d}\Gamma_0. \tag{17}$$

2.4. Dynamics

In dynamic problems, the kinetic energy of the material must be considered. The kinetic energy T can be expressed as

$$T = \int_{\Omega} \frac{1}{2} \rho \dot{\boldsymbol{u}} \cdot \dot{\boldsymbol{u}}\, \mathrm{d}\Omega_0, \tag{18}$$

where ρ is the material density and $\dot{\boldsymbol{u}}$ is the velocity field. According to the Hamiltonian action principle

$$\Pi = \int_{t_0}^{t_1} [T - U]\, \mathrm{d}t \rightarrow STAT, \tag{19}$$

the variational form of Π yields

$$\delta\Pi = \int_{t_0}^{t_1} [\delta T - \delta U]\, \mathrm{d}t = 0. \tag{20}$$

Considering the potential energy defined in Eq. (12), the weak form of the dynamic equilibrium equation can be written as

$$\int_{\Omega} \rho \ddot{\boldsymbol{u}} \cdot \delta\boldsymbol{u}\, \mathrm{d}\Omega_0 + \int_{\Omega} \boldsymbol{S} : \delta\boldsymbol{E}\, \mathrm{d}\Omega_0 = \int_{\Omega} \bar{\boldsymbol{f}} \cdot \delta\boldsymbol{u}\, \mathrm{d}\Omega_0 + \int_{\Gamma_N} \bar{\boldsymbol{t}} \cdot \delta\boldsymbol{u}\, \mathrm{d}\Gamma_0. \tag{21}$$

3. Virtual element method

The most significant feature of the VEM is that it allows the use of polyhedral elements Ω_h to discretize the computational domain Ω. Fig. 2 shows some polyhedral elements that are acceptable in the 3D VEM. We denote by E a polyhedral element, and by $F = \partial E$ its boundary. As shown in Fig. 2, the surface of a polyhedron is composed of polygonal elements with edges denoted by e and vertices denoted by v.

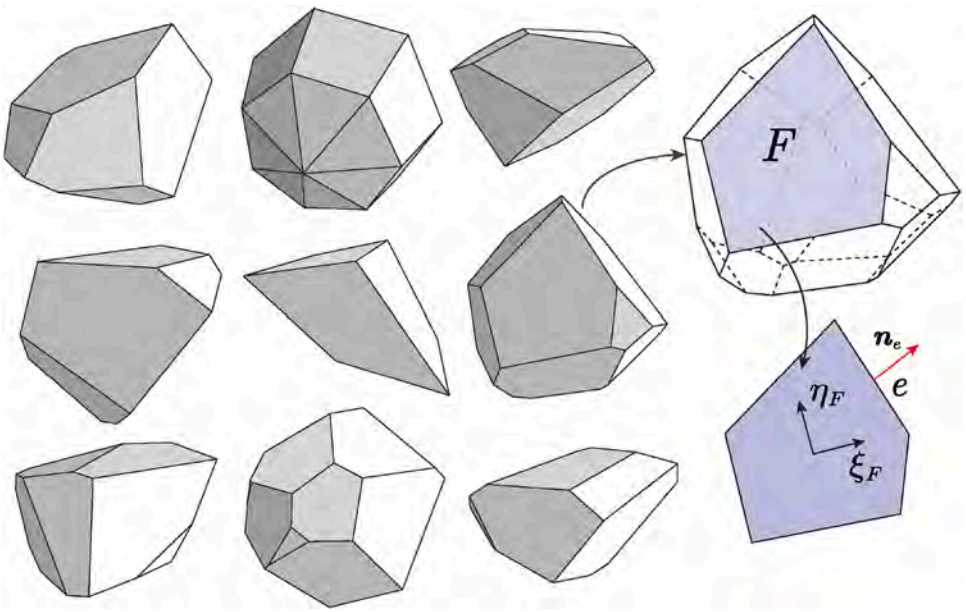

Fig. 2. Some polyhedral elements allowed in 3D virtual element method.

To introduce the S-VEM, we review the classical second-order ($k = 2$) VEM firstly. For polyhedral elements, the basis functions of the virtual element space $\mathcal{V}_k(E)$ are defined indirectly through the projection operator:

$$\Pi_k^{\nabla} : \mathcal{V}_k(E) \to \mathbb{P}_k(E), v \mapsto \Pi_k^{\nabla} v, \tag{22}$$

where Π_k^{∇} is the projection operator, $\mathbb{P}_k(E)$ is the space of polynomials of degree k on E. The local virtual element space on E can be defined as

$$\mathcal{V}_k(E) := \left\{ v \in \mathcal{H}_1 : v|_{\partial E} \in \mathcal{B}(\partial E), \Delta v \in \mathbb{P}_{k-2} \right\}, \tag{23}$$

where $\mathcal{B}(\partial E)$ is the boundary element space for the local polygonal surface element F, see Fig. 2. Different from the two-dimensional VEM, the basis function of the boundary element space is unknown and can be approximated by the local virtual element projection as defined in Eq. (22). Based on the above discussion and definitions, the associated degrees of freedom of the local virtual element space $\mathcal{V}_k(E)$ are

- the values of v_p at the vertices of E;
- the values of the $k-1$ internal Gauss-Lobatto nodes on each edge e of polyhedron E;
- moments on faces F of polyhedron E up to degree $k-2$

$$\frac{1}{|F|} \int_F v p_{k-2}^F \, \mathrm{d}\Omega_F, \quad \forall p_{k-2}^F \in \mathbb{P}_{k-2}(F), \quad \forall \text{face } F \in \partial E; \tag{24}$$

- bulk moments up to degree $k-2$

$$\frac{1}{|E|} \int_E v p_{k-2} \, \mathrm{d}\Omega, \quad \forall p_{k-2} \in \mathbb{P}_{k-2}(E). \tag{25}$$

It is easy to find that for $k = 1$, only the first degree of freedom (values of v_p at the vertices) exists. Since $k = 1$ has a relatively simple format, it is the most widely applied virtual element discretization for mechanical problems. For $k = 2$, the surface moments (moments on faces) and the volume moments (moments in volume) need to be introduced. The local degrees of freedom of the 3D virtual element are shown in Fig. 3 for $k = 1$ and $k = 2$. It can be seen that the number of degrees of freedom of the second-order element increases significantly compared to the first-order element.

According to the basic idea of VEM, for polyhedron element $E \in \Omega_h$, the elliptical projection operator Π_k^{∇} can be obtained from the following orthogonality condition:

$$\begin{cases} \displaystyle\int_E \nabla \Pi_k^{\nabla} v \cdot \nabla p_k \, \mathrm{d}\Omega = \int_E \nabla v \cdot \nabla p_k \, \mathrm{d}\Omega, \quad \forall p_k \in \mathbb{P}_k(E) \\ \displaystyle\int_E \Pi_k^{\nabla} v \, \mathrm{d}\Omega = \int_E v \, \mathrm{d}\Omega. \end{cases} \tag{26}$$

The first equation in Eq. (26) can be expanded as

$$\int_E \nabla \Pi_k^{\nabla} v \cdot \nabla p_k \, \mathrm{d}\Omega = -\int_E v \Delta p_k \, \mathrm{d}\Omega + \sum_{F \in \partial E} \int_F v \frac{\partial p_k}{\partial \boldsymbol{n}_F} \, \mathrm{d}\Gamma, \quad \forall p_k \in \mathbb{P}_k(E), \tag{27}$$

where $\boldsymbol{n}_F$ is the unit normal vector of the polygonal surface element F.

The first term on the right side in Eq. (27) can be calculated using the definition of degrees of freedom. For the second term, the boundary integral is a little more complicated, because we do not know the basis function for the polygonal surface element F. We

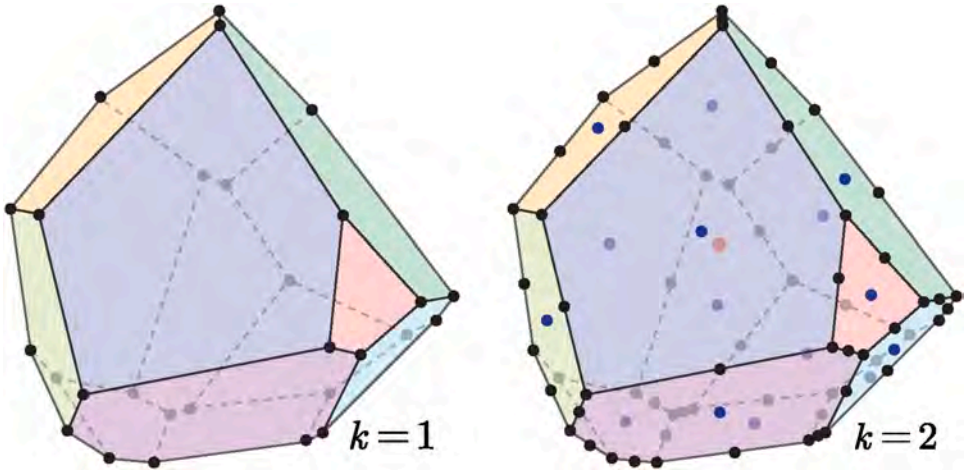

Fig. 3. Local degrees of freedom of the 3D virtual element.

can define a local coordinate (ξ_F, η_F) as shown in Fig. 2 and a local 2D virtual element can be constructed. Then the elliptic projection operator $\Pi^{\nabla}_{k,F}$ for F can be solved based on the degrees of freedom by the following similar orthogonality condition:

$$\begin{cases} \displaystyle\int_F \nabla\Pi^{\nabla}_{k,F} v \cdot \nabla p_k \,\mathrm{d}\Gamma = \int_F \nabla v \cdot \nabla p_k \,\mathrm{d}\Gamma, \quad \forall p_k \in \mathbb{P}_k(E) \\ \displaystyle\int_F \Pi^{\nabla}_{k,F} v \,\mathrm{d}\Omega = \int_E v \,\mathrm{d}\Gamma. \end{cases} \tag{28}$$

Lastly, the boundary integral in Eq. (27) can be approximated as

$$\int_{\partial E} v \frac{\partial p_k}{\partial \boldsymbol{n}_F} \,\mathrm{d}\Gamma = \sum_{F\in\partial E} \int_F \left(\Pi^{\nabla}_{k,F} v\right) \frac{\partial p_k}{\partial \boldsymbol{n}_F} \,\mathrm{d}\Gamma. \tag{29}$$

The identity here above represents in principle an approximation of the exact integral since the correct projector would be the L^2 projection on polynomials. Nevertheless the same identity can also be interpreted as an exact calculation by introducing a suitable modification of the virtual boundary space definition; see for instance Section 3.6 of [40]. Substituting the projection operator Π^{∇}_k (obtained by solving the orthogonality condition Eq. (26)) into the weak form Eq. (15) and considering the stabilization term yields the local approximations of the bilinear form. Here we only consider the projection operator. The discrete counterpart of the weak form in Eq. (13) and the choice of stabilization terms will be explained in detail in the following section.

4. Serendipity virtual element method

The S-VEM is a special format of the VEM, which reduces the number of degrees of freedom of the higher-order virtual element. As mentioned before, the boundary of the 3D virtual element is composed of polygonal elements and the projection operator Π^{∇}_k is calculated based on the local 2D virtual element. Therefore, in order to eliminate the surface moment, we should first consider the two-dimensional serendipity virtual element.

4.1. Serendipity virtual elements on faces

Consider the polyhedral element and its polygonal surfaces as shown in Fig. 4. Serendipity virtual elements are based on the introduction of a projection operator

$$\Pi^{S}_{k,F} : \mathcal{V}_k(F) \to \mathbb{P}_k(F), v \mapsto \Pi^{S}_{k,F} v, \tag{30}$$

where $\mathcal{V}_k(F)$ is the standard virtual element space on the polygonal surface F. Basically, the projection operator can be computed using only the boundary degrees of freedom and another face degrees of freedom up to order β_F, where $\beta_F := k - \eta^F$, η^F is the

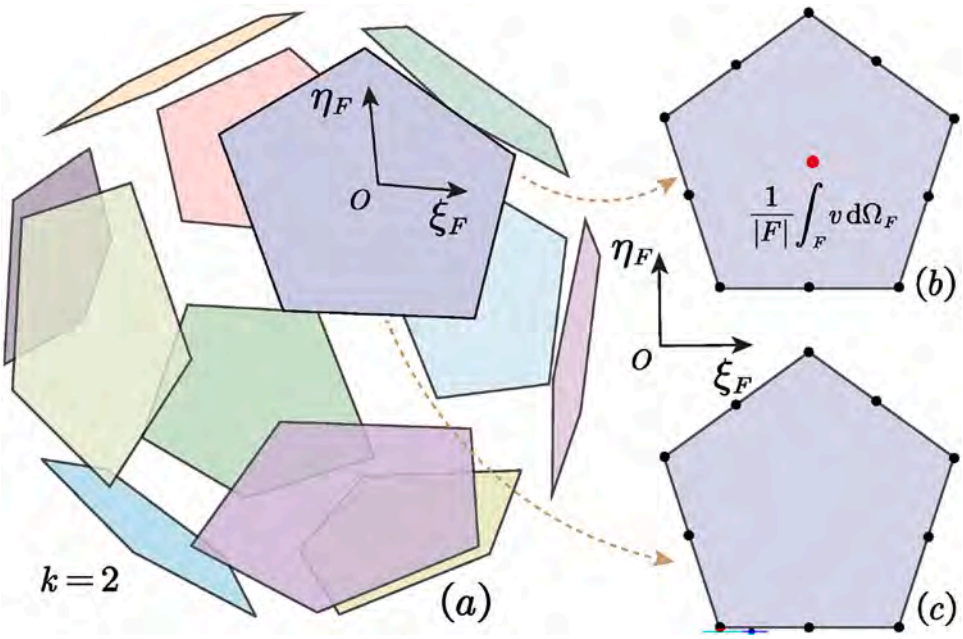

Fig. 4. Face element for classical VEM and S-VEM, (a): polyhedral element and its polygonal surfaces; (b): degrees of freedom of the classical 2D VEM; (c): degrees of freedom of the serendipity 2D VEM.

number of distinct straight lines that contain at least one edge of F [36]. Since $\eta^F \geq 3$ for any polygonal surface, we will never need internal moments for $k = 2$. The degrees of freedom of the serendipity virtual element F are shown in Fig. 4 for $k = 2$.

Based on the above assumptions, the serendipity projection operator $\Pi^S_{k,F}$ is defined by

$$\int_{\partial F} \Pi^S_{k,F} v p \, \mathrm{d}\Gamma = \int_{\partial F} v p \, \mathrm{d}\Gamma \quad \forall p \in \mathbb{P}_k(F). \tag{31}$$

Considering the basis function $\boldsymbol{\phi}$ of the serendipity virtual element space $\mathcal{V}^S_k(F)$ and the scaled basis function $\boldsymbol{m}$ of the polynomial space $\mathbb{P}_k$, yields

$$\int_{\partial F} \boldsymbol{m}\boldsymbol{m}^T \, \mathrm{d}\Gamma \boldsymbol{\Pi}^{S*}_{k,F} = \int_{\partial F} \boldsymbol{m}\boldsymbol{\phi}^T \, \mathrm{d}\Gamma \Rightarrow \boldsymbol{H}_{edge}\boldsymbol{\Pi}^{S*}_{k,F} = \boldsymbol{C}_{edge}, \tag{32}$$

where $\boldsymbol{\Pi}^{S*}_{k,F}$ is the matrix form of the serendipity projection operator, and

$$\boldsymbol{H}_{edge} := \int_{\partial F} \boldsymbol{m}\boldsymbol{m}^T \, \mathrm{d}\Gamma, \quad \boldsymbol{C}_{edge} := \int_{\partial F} \boldsymbol{m}\boldsymbol{\phi}^T \, \mathrm{d}\Gamma. \tag{33}$$

The basis funciton on the edge e is exactly known based on the Lagrange interpolation. Therefore, the serendipity projection operator on face can be solved by

$$\boldsymbol{\Pi}^{S*}_{k,F} = \boldsymbol{H}^{-1}_{edge}\boldsymbol{C}_{edge}. \tag{34}$$

Note that there exist some other choices of the projection operator $\Pi^S_{k,F}$ as mentioned in [36,38].

4.2. Serendipity virtual elements on polyhedrons

Based on the serendipity virtual element on faces, we can define the serendipity virtual element on polyhedrons. The simplest way is to use the elliptical projection $\Pi^\nabla_k(E)$ in the conventional VEM. We define the following boundary space

$$\mathcal{B}^S_k(\partial E) := \left\{ v \in C^0(\partial E) : v|_F \in \mathcal{V}^S_k(F), \quad \forall F \in \partial E \right\}. \tag{35}$$

We do not detail here the definition of the face spaces $\mathcal{V}^S_k(F)$, which are (as usual) built as functions which are piecewise polynomials of degree k on ∂F and that satisfy a suitable elliptic equation inside F; the interested reader can check [36,37]. Once the boundary space is defined, we can construct the local virtual space as well as the projection operators for 3D element E. The approach is to use the projection operator Π^∇_k to project the function v into the polynomial space $\mathbb{P}_k(E)$. Then the local virtual element space can be defined as

$$\mathcal{V}^S_k(E) := \left\{ v \in \mathcal{H}_1 : v|_{\partial E} \in \mathcal{B}^S_k(\partial E), \Delta v \in \mathbb{P}_{k-2} \right\}. \tag{36}$$

Based on these definations, the elliptical projection operator $\Pi^{\nabla S}_k$ for the serendipity element can be solved by the orthogonality condition Eq. (26):

$$\begin{cases} \displaystyle\int_E \nabla \Pi^{\nabla S}_k v \cdot \nabla p_k \, \mathrm{d}\Omega = \int_E \nabla v \cdot \nabla p_k \, \mathrm{d}\Omega, \quad \forall p_k \in \mathbb{P}_k(E) \\ \displaystyle\int_E \Pi^{\nabla S}_k v \, \mathrm{d}\Omega = \int_E v \, \mathrm{d}\Omega. \end{cases} \tag{37}$$

To distinguish from the projection operator Π^∇_k in Eq. (26), we use $\Pi^{\nabla S}_k$ to represent the elliptical projection operator for the serendipity element. The first equation in Eq. (37) can be expanded as

$$\int_E \nabla \Pi^{\nabla S}_k v \cdot \nabla p_k \, \mathrm{d}\Omega = -\int_E v \Delta p_k \, \mathrm{d}\Omega + \sum_{F \in \partial E} \int_F \left(\Pi^S_{k,F} v \right) \frac{\partial p_k}{\partial \boldsymbol{n}_F} \, \mathrm{d}\Gamma. \tag{38}$$

It is easy to check that a set of degrees of freedom for the space $\mathcal{V}^S_k(E)$ is given by

- the values of v_p at the vertices of E;
- the values of the $k-1$ internal Gauss-Lobatto nodes on each edge e of polyhedron $F \in \partial E$;
- bulk moments up to degree $k-2$

$$\frac{1}{|E|} \int_E v p_{k-2} \, \mathrm{d}\Omega, \quad \forall p_{k-2} \in \mathbb{P}_{k-2}(E). \tag{39}$$

Note that for arbitrary k, another set of degrees of freedom has to defined by [36–38]:

- face moments up to degree $k - \eta^F$

$$\frac{1}{|F|} \int_E v p_{k-\eta^F} \, \mathrm{d}\Omega, \quad \forall p_{k-\eta^F} \in \mathbb{P}_{k-\eta^F}(F) \quad \forall F \in \partial E, \tag{40}$$

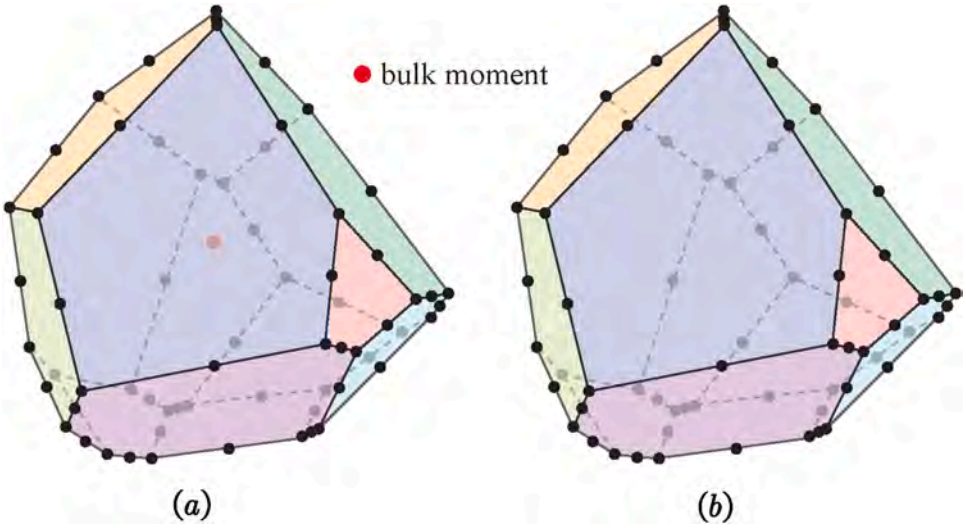

Fig. 5. Local degrees of freedom of the 3D serendipity virtual element, (a): serendipity element with bulk moment; (b): serendipity element without bulk moment.

where η^F is the number of distinct straight lines that contain at least one edge of F, as discussed in [36–38]. Furthermore, in such case also identity Eq. (38) should be partially changed. Fortunately, there is no such degree of freedom ($\eta^F \geq 3$) if we only consider $k = 2$, so that we can avoid changing Eq. (38) and avoid adding the face moment DoFs here above.

Lastly, the matrix formulation of the Ritz projection operator $\mathbf{\Pi}_{k,E}^{\nabla,S*}$ can be solved by

$$\begin{cases} \boldsymbol{G}\mathbf{\Pi}_{k,E}^{\nabla,S*} = \boldsymbol{B} \\ \int_E \boldsymbol{m}^T \,\mathrm{d}\Omega \mathbf{\Pi}_{k,E}^{\nabla,S*} = \int_E \boldsymbol{\phi}^T \,\mathrm{d}\Omega, \end{cases} \tag{41}$$

where

$$\boldsymbol{G} = \int_E \nabla \boldsymbol{m} \cdot \nabla \boldsymbol{m}^T \,\mathrm{d}\Omega, \tag{42}$$

$$\boldsymbol{B} = -\int_E \Delta \boldsymbol{m} \cdot \boldsymbol{\phi}^T \,\mathrm{d}\Omega + \sum_{F \subset \partial E} \int_F (\nabla \boldsymbol{m} \cdot \boldsymbol{n}_F) \boldsymbol{m}_F^T \,\mathrm{d}\Gamma \mathbf{\Pi}_{k,F}^{\nabla,S*}. \tag{43}$$

In this format, we observe that there are still extra degrees of freedom inside (bulk moments up to degree $k-2$) in the current situation. For the case of $k = 2$, the number of internal degrees of freedom is 1, as shown in Fig. 5(a).

In order to remove the internal degrees of freedom, we construct a serendipity space and a serendipity projection operator $\Pi_{k,E}^S$ (or "boundary" projector) for the three-dimensional element similar to the projection defined in Eq. (31)

$$\int_{\partial E} \Pi_{k,E}^S v p \,\mathrm{d}\Gamma = \int_{\partial E} v p \,\mathrm{d}\Gamma, \quad \forall p \in \mathbb{P}_k(E). \tag{44}$$

Note that for $k = 2$ the equation here above always has a unique solution (such property would be false for very high k but could be corrected introducing suitable volume moments). Then the matrix form of the boundary projection operator $\mathbf{\Pi}_{k,E}^{S*}$ can be solved by

$$\int_{\partial E} \boldsymbol{m}\boldsymbol{m}^T \,\mathrm{d}\Gamma \mathbf{\Pi}_{k,E}^{S*} = \int_{\partial E} \boldsymbol{m}\boldsymbol{\phi}^T \,\mathrm{d}\Gamma \Rightarrow \boldsymbol{H}_{face} \mathbf{\Pi}_{k,E}^{S*} = \boldsymbol{C}_{face}, \tag{45}$$

It is easy to find, for $k = 2$, that the degrees of freedom are given by

- the values of v_p at the vertices of E;
- the values of the $k-1$ internal Gauss-Lobatto nodes on each edge e of polyhedron $F \in \partial E$.

Based on the boundary projection operator $\Pi_{k,E}^S$, the missing moments in Eq. (43) can be computed and the Ritz projection operator $\Pi_{k,E}^{\nabla,S*}$ is obtained.

Through the above two approaches, we have two formats for calculating the projection operator. Both formats delete the moments on the element faces, but the second format further deletes the volume moments. For $k = 2$, the degree of freedom distributions for different approaches are shown in Fig. 5.

The results obtained by different projection operators will be analyzed in detail in the numerical examples.

5. Serendipity virtual element method for hyperelasticity

The projection operators derived above will be used to construct the discrete format of the hyperelastic problem. Therefore, in order to avoid conflicts, we uniformly use $\Pi^{\nabla S}_{k,E}$ (with matrix form $\mathbf{\Pi}^{\nabla S}_{k,E}$) to represent the projection for the 3D serendipity element.

5.1. Incremental formulation of hyperelasticity

The discrete format of the hyperelastic problem can be obtained based on the nonlinear continuum mechanics framework. Considering the internal virtual work in a Lagrangian form as

$$\mathcal{W} = \int_\Omega \delta \boldsymbol{E} : \boldsymbol{S} \, \mathrm{d}\Omega_0, \tag{46}$$

the linearization of the virtual work is obtained as

$$\Delta\mathcal{W} = \int_\Omega \delta \boldsymbol{E} : \Delta \boldsymbol{S} \, \mathrm{d}\Omega_0 + \int_\Omega \Delta(\delta \boldsymbol{E}) : \boldsymbol{S} \, \mathrm{d}\Omega_0. \tag{47}$$

With the definition of the Green-Lagrange strain $\boldsymbol{E}$ in Eq. (3) and the second Piola-Kirchhoff stress tensor $\boldsymbol{S}$ in Eq. (9), it follows

$$\begin{aligned} \Delta\mathcal{W} &= \int_\Omega \delta \boldsymbol{E} : \Delta \boldsymbol{S} \, \mathrm{d}\Omega_0 + \int_\Omega \boldsymbol{S} : \left(\delta \boldsymbol{D}^T \cdot \Delta \boldsymbol{D}\right) \mathrm{d}\Omega_0 \\ &= \int_\Omega \delta \boldsymbol{E} : \boldsymbol{\mathcal{D}} : \Delta \boldsymbol{E} \, \mathrm{d}\Omega_0 + \int_\Omega \boldsymbol{S} : \left(\delta \boldsymbol{D}^T \cdot \Delta \boldsymbol{D}\right) \mathrm{d}\Omega_0, \end{aligned} \tag{48}$$

where $\boldsymbol{\mathcal{D}}$ is the tangential material tensor (see Eq. (10) for the compressible Non-Hookean material) and $\boldsymbol{D} = \frac{\partial \boldsymbol{u}}{\partial \boldsymbol{X}}$ is the displacement gradient. Then we can define

$$\boldsymbol{S} : \left(\delta \boldsymbol{D}^T \cdot \Delta \boldsymbol{D}\right) = \delta \boldsymbol{\theta}^T \cdot \boldsymbol{\mathcal{I}} \cdot \Delta \boldsymbol{\theta}, \tag{49}$$

where

$$\boldsymbol{\theta} = \left[\frac{\partial u}{\partial X} \quad \frac{\partial u}{\partial Y} \quad \frac{\partial u}{\partial Z} \quad \frac{\partial v}{\partial X} \quad \frac{\partial v}{\partial Y} \quad \frac{\partial v}{\partial Z} \quad \frac{\partial w}{\partial X} \quad \frac{\partial w}{\partial Y} \quad \frac{\partial w}{\partial Z}\right]^T, \quad \boldsymbol{\mathcal{I}} = \mathrm{diag}(\boldsymbol{S}, \boldsymbol{S}, \boldsymbol{S}). \tag{50}$$

Utilization Voigt notation, the linearization of the virtual work has the form as

$$\Delta\mathcal{W} = \int_\Omega \delta \boldsymbol{\theta}^T \cdot \left(\boldsymbol{A}^T \cdot \hat{\boldsymbol{D}} \cdot \boldsymbol{A} + \boldsymbol{\mathcal{I}}\right) \cdot \Delta \boldsymbol{\theta} \, \mathrm{d}\Omega_0, \tag{51}$$

where $\hat{\boldsymbol{D}}$ is the constitutive matrix in Voigt notation of $\boldsymbol{\mathcal{D}}$. The matrix $\boldsymbol{A}$ is the gradient operator matrix, which is defined as

$$\boldsymbol{A} = \begin{bmatrix} F_{11} & 0 & 0 & F_{21} & 0 & 0 & F_{31} & 0 & 0 \\ 0 & F_{12} & 0 & 0 & F_{22} & 0 & 0 & F_{32} & 0 \\ 0 & 0 & F_{13} & 0 & 0 & F_{23} & 0 & 0 & F_{33} \\ F_{12} & F_{11} & 0 & F_{22} & F_{21} & 0 & F_{32} & F_{31} & 0 \\ 0 & F_{13} & F_{12} & 0 & F_{23} & F_{22} & 0 & F_{33} & F_{32} \\ F_{13} & 0 & F_{11} & F_{23} & 0 & F_{21} & F_{33} & 0 & F_{31} \end{bmatrix}. \tag{52}$$

5.2. Discrete format

We introduced different projection operators for the S-VEM in Section 4.2. The projection operator $\Pi^{S}_{k,E}$ can be used to construct the discrete format of the hyperelastic problem. Note that the displacement $\boldsymbol{u} = [u_x, u_y, u_z]^T$ is a vector, we can define a vector serendipity projection operator

$$\Pi^{\nabla S}_{k,\boldsymbol{u}} : \boldsymbol{\mathcal{V}}_k(E) \to \left(\mathbb{P}_k(E)\right)^3, \quad \boldsymbol{v} \mapsto \Pi^{\nabla S}_{k,\boldsymbol{u}} \boldsymbol{v}. \tag{53}$$

The projection $\Pi^{\nabla S}_{k,\boldsymbol{u}}$ can be obtained directly by $\Pi^{\nabla S}_{k,\boldsymbol{u}} = \Pi^{\nabla S}_{k} \otimes \mathbb{I}_3$ where $\Pi^{\nabla S}_{k}$ is the serendipity projection operator and $\mathbb{I}_3$ is the 3×3 order identity matrix, $\otimes$ is the Kronecker product.

Based on the principle of the VEM, the displacement field $\boldsymbol{u}$ can be split into $\Pi^{\nabla S}_{k,\boldsymbol{u}} \boldsymbol{u}_h$ and a remainder $\boldsymbol{u}_h - \Pi^{\nabla S}_{k,\boldsymbol{u}} \boldsymbol{u}_h$ as

$$\boldsymbol{u}_h = \Pi^{\nabla S}_{k,\boldsymbol{u}} \boldsymbol{u}_h + \left(\boldsymbol{u}_h - \Pi^{\nabla S}_{k,\boldsymbol{u}} \boldsymbol{u}_h\right). \tag{54}$$

By expanding the projection operator in different spaces, we obtain

$$\begin{aligned} \boldsymbol{u}_h &= \boldsymbol{\phi}^T_{\boldsymbol{u}} \mathbf{\Pi}^{\nabla S}_{k,\boldsymbol{u}} \tilde{\boldsymbol{u}}_h + \boldsymbol{\phi}^T_{\boldsymbol{u}} \left(\boldsymbol{I}_K - \mathbf{\Pi}^{\nabla S}_{k,\boldsymbol{u}}\right) \tilde{\boldsymbol{u}}_h \\ &= \boldsymbol{m}^T_{\boldsymbol{u}} \mathbf{\Pi}^{\nabla S*}_{k,\boldsymbol{u}} \tilde{\boldsymbol{u}}_h + \boldsymbol{\phi}^T_{\boldsymbol{u}} \left(\boldsymbol{I}_K - \mathbf{\Pi}^{\nabla S*}_{k,\boldsymbol{u}}\right) \tilde{\boldsymbol{u}}_h, \end{aligned} \tag{55}$$

where $\boldsymbol{\phi}_{\boldsymbol{u}}$ and $\boldsymbol{m}_{\boldsymbol{u}}$ are the basis functions for $\boldsymbol{\mathcal{V}}_k(E)$ and $\left(\mathbb{P}_k(E)\right)^3$, individually. In addition, $\boldsymbol{I}_K$ is an identity matrix that has the same size as the number of degrees of freedom in the element E, $\tilde{\boldsymbol{u}}$ is the displacement vector for each node of the element.

Based on Eq. (55), the displacement gradient $\boldsymbol{\theta}_h$ can be written as

$$\boldsymbol{\theta}_h = \nabla \boldsymbol{m}_{\boldsymbol{u}}^T \boldsymbol{\Pi}_{k,\boldsymbol{u}}^{\nabla S*} \tilde{\boldsymbol{u}}_h + \nabla \boldsymbol{\phi}_{\boldsymbol{u}}^T \left(\boldsymbol{I}_K - \boldsymbol{\Pi}_{k,\boldsymbol{u}}^{\nabla S*} \right) \tilde{\boldsymbol{u}}_h. \tag{56}$$

Substituting Eq. (56) into Eq. (51), the linearization of the virtual work follows

$$\begin{aligned} \Delta \mathcal{W} = {} & \delta \tilde{\boldsymbol{u}}_h^T \left(\boldsymbol{\Pi}_{k,\boldsymbol{u}}^{\nabla S*} \right)^T \int_\Omega \nabla \boldsymbol{m}_{\boldsymbol{u}} \left(\boldsymbol{A}^T \cdot \hat{\boldsymbol{D}} \cdot \boldsymbol{A} + \boldsymbol{I} \right) \nabla \boldsymbol{m}_{\boldsymbol{u}}^T \, \mathrm{d}\Omega_0 \boldsymbol{\Pi}_{k,\boldsymbol{u}}^{\nabla S*} \Delta \tilde{\boldsymbol{u}}_h \\ & + \delta \tilde{\boldsymbol{u}}^T \left(\boldsymbol{I}_K - \boldsymbol{\Pi}_{k,\boldsymbol{u}}^{\nabla S*} \right)^T \int_\Omega \nabla \boldsymbol{\phi}_{\boldsymbol{u}} \left(\boldsymbol{A}^T \cdot \hat{\boldsymbol{D}} \cdot \boldsymbol{A} + \boldsymbol{I} \right) \nabla \boldsymbol{\phi}_{\boldsymbol{u}}^T \, \mathrm{d}\Omega_0 \left(\boldsymbol{I}_K - \boldsymbol{\Pi}_{k,\boldsymbol{u}}^{\nabla S*} \right) \Delta \tilde{\boldsymbol{u}}. \end{aligned} \tag{57}$$

Then the element tangent stiffness matrix is obtained as

$$\boldsymbol{K} = \boldsymbol{K}_c + \boldsymbol{K}_s, \tag{58}$$

with the consistant part

$$\boldsymbol{K}_c = \left(\boldsymbol{\Pi}_{k,\boldsymbol{u}}^{\nabla S*} \right)^T \int_\Omega \nabla \boldsymbol{m}_{\boldsymbol{u}} \left(\boldsymbol{A}^T \cdot \hat{\boldsymbol{D}} \cdot \boldsymbol{A} + \boldsymbol{I} \right) \nabla \boldsymbol{m}_{\boldsymbol{u}}^T \, \mathrm{d}\Omega_0 \boldsymbol{\Pi}_{k,\boldsymbol{u}}^{\nabla S*} \tag{59}$$

the stabilization term

$$\boldsymbol{K}_s = \left(\boldsymbol{I}_K - \boldsymbol{\Pi}_{k,\boldsymbol{u}}^{\nabla S*} \right)^T \int_\Omega \nabla \boldsymbol{\phi}_{\boldsymbol{u}} \left(\boldsymbol{A}^T \cdot \hat{\boldsymbol{D}} \cdot \boldsymbol{A} + \boldsymbol{I} \right) \nabla \boldsymbol{\phi}_{\boldsymbol{u}}^T \, \mathrm{d}\Omega_0 \left(\boldsymbol{I}_K - \boldsymbol{\Pi}_{k,\boldsymbol{u}}^{\nabla S*} \right). \tag{60}$$

It is complicated to calculate the stabilization term $\boldsymbol{K}_s$ directly since we never know the basis function $\boldsymbol{\phi}_{\boldsymbol{u}}$. Considering $\int_{V_0} \nabla \boldsymbol{\phi}_{\boldsymbol{u}} \nabla \boldsymbol{\phi}_{\boldsymbol{u}}^T \approx \mathcal{O}(1)$, the stabilization term can be approximated as

$$\boldsymbol{K}_s = \alpha \left(\boldsymbol{I}_K - \boldsymbol{\Pi}_{k,\boldsymbol{u}}^{\nabla S} \right)^T \left(\boldsymbol{I}_K - \boldsymbol{\Pi}_{k,\boldsymbol{u}}^{\nabla S} \right), \tag{61}$$

where α is a stabilization parameter that can be adjusted to improve the stability of the solution. Note that a very small parameter α may degenerate the stability properties of the numerical scheme, while a very large parameter α may result in an artificial over-stiffness; nevertheless, in general there is a wide range of choices for α that guarantee good results. Based on previous work, the stability parameter can be chosen as

$$\alpha = \frac{1}{d^2} \mathrm{tr}(\hat{\boldsymbol{D}}) = \frac{4}{9} \mathrm{tr}\left(\frac{\partial^2 \Psi}{\partial \boldsymbol{C} \partial \boldsymbol{C}} \right), \quad d = 3. \tag{62}$$

The internal force has the form

$$\boldsymbol{F}_{\mathrm{int}} = \left(\boldsymbol{\Pi}_{k,\boldsymbol{u}}^{\nabla S*} \right)^T \int_{V_0} \nabla \boldsymbol{m}_{\boldsymbol{u}} \boldsymbol{A}^T \hat{\boldsymbol{S}} \, \mathrm{d}V_0 + \boldsymbol{F}_{\mathrm{int}}^s, \tag{63}$$

where $\hat{\boldsymbol{S}}$ is the second Piola-Kirchhff stress tensor in Voigt notation, $\boldsymbol{F}_{\mathrm{int}}^s$ is the stabilization term for internal force. It can be approximated by

$$\boldsymbol{F}_{\mathrm{int}}^s = \boldsymbol{K}_s \boldsymbol{U}_t. \tag{64}$$

6. Dynamic problem

For the dynamic problem of the hyperelasticity, the weak form of the momentum equation is given in Eq. (21). Insertion of the serendipity projection into the inertia term in Eq. (21), the mass matrix can be obtained as

$$\boldsymbol{M} = \rho \left(\boldsymbol{\Pi}_{k,\boldsymbol{u}}^{\nabla S*} \right)^T \int_\Omega \boldsymbol{m}_{\boldsymbol{u}} \boldsymbol{m}_{\boldsymbol{u}}^T \, \mathrm{d}\Omega_0 \boldsymbol{\Pi}_{k,\boldsymbol{u}}^{\nabla S*} + \boldsymbol{M}_s, \tag{65}$$

where $\boldsymbol{M}_s$ is the stabilization term for the mass matrix, which can be approximated as

$$\boldsymbol{M}_s = \rho |E| \left(\boldsymbol{I}_K - \boldsymbol{\Pi}_{k,\boldsymbol{u}}^{\nabla S} \right)^T \left(\boldsymbol{I}_K - \boldsymbol{\Pi}_{k,\boldsymbol{u}}^{\nabla S} \right), \tag{66}$$

where $|E|$ is the volume of the element E. Note that using the projection operator $\boldsymbol{\Pi}_{k,\boldsymbol{u}}^{\nabla S*}$ to compute $\boldsymbol{M}$ (insted of the natural choice which would be an L^2 type projection operator) can be justified by a suitable modification of the definition of the virtual space inside the element E.

Considering the mass matrix $\boldsymbol{M}$ and the stiffness matrix $\boldsymbol{K}$, the balance equation for the dynamic analysis is

$$\boldsymbol{M} \ddot{\boldsymbol{u}}_{(t+\Delta t)} + \boldsymbol{K}_{(t)} \boldsymbol{u} = \boldsymbol{F}_{(t+\Delta t)} - \boldsymbol{F}_{\mathrm{int},(t)}. \tag{67}$$

For the solution of the time dependent nonlinear problem, the Newmark method will be applied which can be written as

$$\left(\boldsymbol{K}_{(t)} + \frac{1}{\beta \Delta t^2} \boldsymbol{M} \right) \Delta \boldsymbol{u}_{(t)} = \boldsymbol{F}_{(t+\Delta t)} - \boldsymbol{F}_{\mathrm{int},(t)} - \boldsymbol{F}_{\mathrm{dyna}}, \tag{68}$$

where

$$\boldsymbol{F}_{\mathrm{dyna}} = \boldsymbol{M} \left[\frac{1}{\beta \Delta t^2} \left(\boldsymbol{u}_{(t+\Delta t)} - \boldsymbol{u}_{(t)} \right) - \frac{1}{\beta \Delta t} \dot{\boldsymbol{u}}_{(t)} - \left(\frac{1}{2\beta} - 1 \right) \ddot{\boldsymbol{u}}_{(t)} \right]. \tag{69}$$

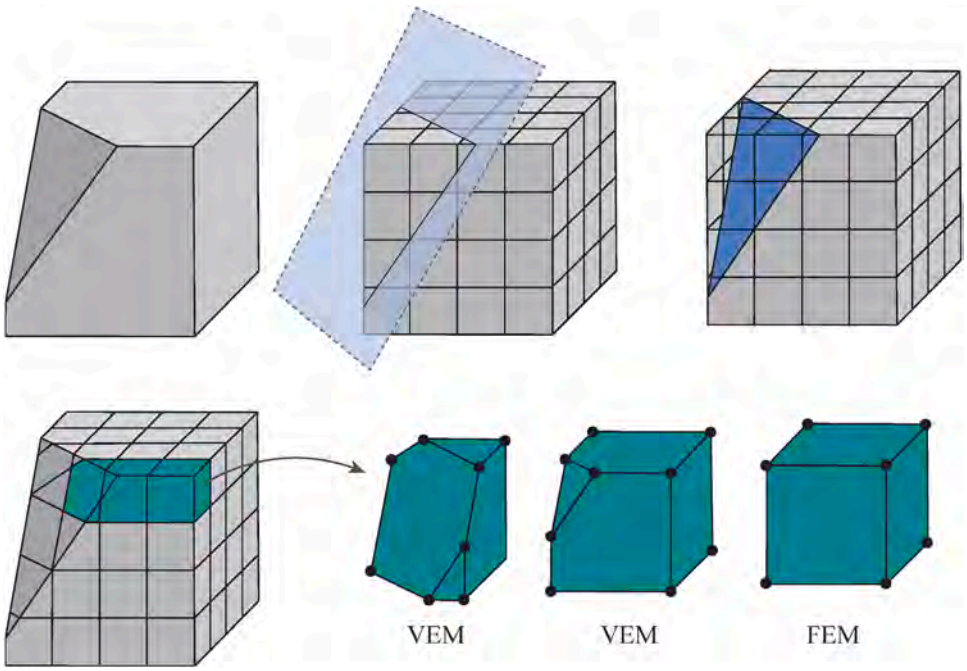

Fig. 6. Mesh generation based on the trimmed hexahedral meshes.

For each time step, after the result reaches convergence, the velocity and acceleration can be updated by

$$\ddot{\boldsymbol{u}}_{(t+\Delta t)} = \frac{1}{\beta(\Delta t)^2}\left[\boldsymbol{u}_{(t+\Delta t)} - \boldsymbol{u}_{(t)} - \dot{\boldsymbol{u}}_{(t)}\Delta t - \left(\frac{1}{2} - \beta\right)(\Delta t)^2\ddot{\boldsymbol{u}}_{(t)}\right], \tag{70}$$

$$\dot{\boldsymbol{u}}_{(t+\Delta t)} = \dot{\boldsymbol{u}}_{(t)} + \left[(1-\gamma)\ddot{\boldsymbol{u}}_{(t)} + \gamma\ddot{\boldsymbol{u}}_{(t+\Delta t)}\right]\Delta t, \tag{71}$$

where β and γ are the Newmark parameters, and they can be chosen as $\beta = 0.25$ and $\gamma = 0.5$ for an implicit time integration. If convergence difficulties are encountered during the nonlinear iteration process, the time step has to be reduced and then the calculation has to be restarted from the last convergence step.

7. VEM-FEM hybrid formats

Often, hexahedral or hexahedral-dominant meshes have better numerical stability and accuracy than tetrahedral meshes in the finite element analysis. However, hexahedral mesh generation is challenging, especially for complex geometry [41–43]. The grid-based trimmed hexahedral (TH) meshing algorithm [44,45] is a good choice for generating hexahedral-dominant meshes for complex geometry. But at the same time, trimmed polyhedral elements are generated at the boundary of the model, as shown in Fig. 6.

In order to improve the adaptability to geometries with curved surfaces and sharp parts, the VoroCrust algorithm [46] is used to generate a mesh that can handle a large class of domains with both curved boundaries and arbitrarily sharp features. The interior can use Cartesian hexahedral meshes, while the surface uses triangle discretization, which is suitable for complex geometries. In the transition zone, tetraheda or polyhedra are employed for transition. The grid obtained by using such ideas is shown in Fig. 7.

Based on the above discussion, we can consider hybrid formats to improve the accuracy and efficiency of complex geometric structures. We use the finite element method for the internal hexahedral mesh and the virtual element method for the surface polyhedral mesh. For 2D problems, finite elements and virtual elements on edges correspond exactly (both being polynomials). For 3D problems, the elimination of surface degrees of freedom enables the second-order VEM to be coupled with the second-order serendipity FEM (Q20), simply by a standard gluing of the face degrees of freedom which, on quadrilateral faces, are the same for FEM and Serendipity VEM. On the other hand we must note that the rigorous definition of the two spaces are not identical on such faces (FEM are bivariate polynomials of order 2, while VEM are defined through a suitable equation on the element); nevertheless this small non-conformity “crime” introduces a negligible error in the computations. Of course, for more general meshes, we can use triangular meshes on the coupling surfaces. However, this will lead to two problems: FEM requires the use of tetrahedral elements, and the triangle elements will increase the number of degrees of freedom.

This hybrid format allows the use of directly generated hexahedral-dominant meshes and improves the stability of the simulation. The VEM is also used for the elements with hanging nodes generated during the adaptive process, see Fig. 7. This simulation format facilitates efficient analysis of industrial problems.

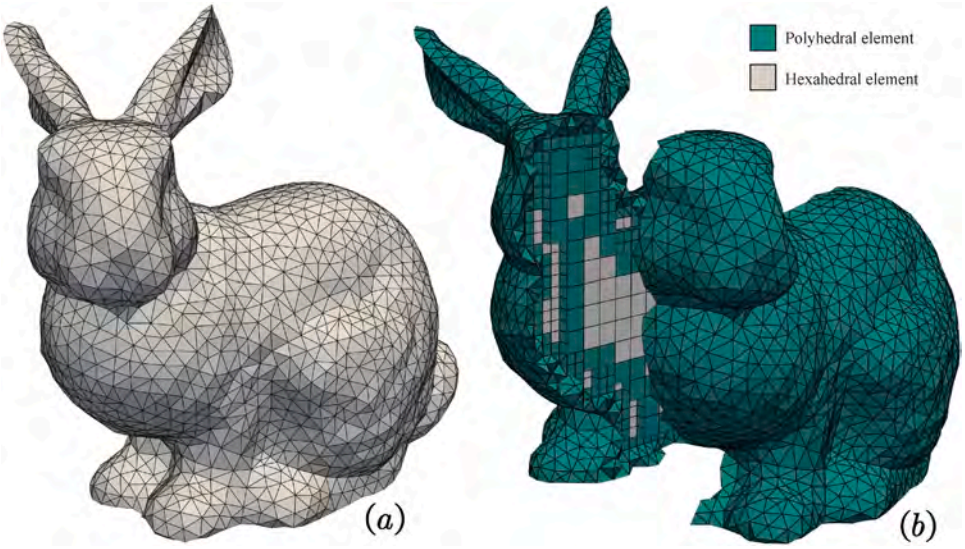

Fig. 7. The rabbit model for the VEM-FEM coupling technique.

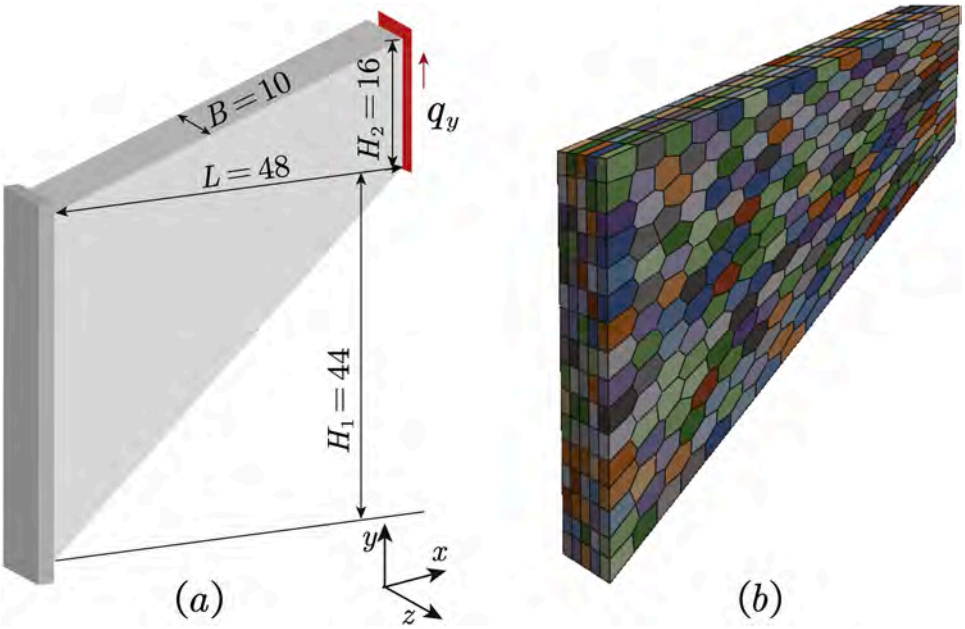

Fig. 8. 3D Cook's membrane: (a) geometry and boundary conditions, (b) polyhedral mesh.

Table 1
Maximum displacements u_y for different discretizations under $q_y = 4$. In the FEM, we use a hexahedral mesh with the same density.

	VEM		FEM		S-VEM ($k = 2$)	
N	$k = 1$	$k = 2$	H1	H2	with bulk moment	without bulk moment
2	9.6363	11.2741	8.62856	11.162	11.1417	11.0580
3	10.7117	11.2943	10.3517	11.2515	11.2369	11.1930
4	11.0981	11.2943	11.0072	11.2828	11.2868	11.2794
5	11.2351	11.3027	11.2099	11.2974	11.2968	11.2895

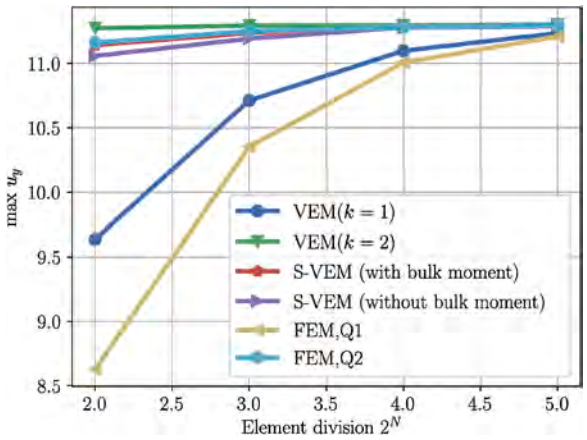

Fig. 9. Maximum displacement u_y obtained by different methods with different discretizations.

Table 2
Total degrees of freedom for different discretizations.

	VEM		S-VEM ($k=2$)	
N	$k=1$	$k=2$	with bulk moment	without bulk moment
2	684	3,663	2514	2,244
3	2,178	11,913	8133	7,233
4	8,388	46,167	31,470	27,960
5	36,594	201,729	137,457	122,097

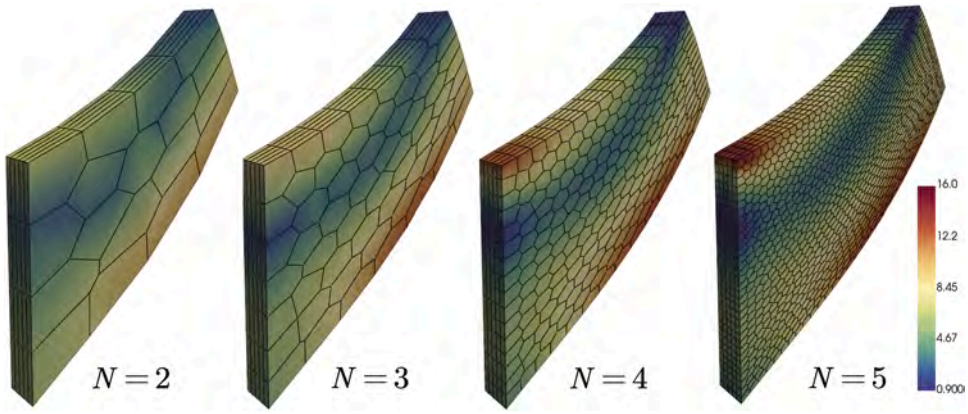

Fig. 10. Contour plots of von-Mises stresses for different meshes.

8. Numerical examples

8.1. Cook's membrane problem

As a first example, we will test the convergence of the serendipity VEM. As shown in Fig. 8, a Cook's membrane problem under quasi-static loading condition is given. The dimensions are $H_1 = 44$, $H_2 = 16$, $L = 48$, and $B = 10$.

A Neo-Hookean model is selected with the material parameters are $\lambda = 100$ and $\mu = 40$. The Cook's membrane is fixed on the left side and traction $q_y = 4$ is applied on the right side. To test the accuracy and convergence of the S-VEM, different mesh discretizations are selected with parameter N. As shown in Fig. 8, the geometry is divided into $2^N \times 2^N$ elements in the vertical and horizontal directions. To compare the results, the conventional FEM (FEM H1 and H2) and VEM ($k = 1$ and $k = 2$ with additional moments) are selected for comparison. Of course, we use a polyhedral mesh in VEM as shown in Fig. 8 and hexahedral mesh of the same density in FEM.

The maximum displacement u_y for different discretizations obtained by different methods is listed in Table 1. The convergence lines are given in Fig. 9. Clearly, the solutions obtained by S-VEM matchtes very vell with the solutions obtained by FEM with H2 element. In addition, the S-VEM with bulk moment has better accuracy and convergence.

Table 3
The vertical displacement u_z of point A for different discretizations ("poly" represents a polyhedral element, "hexa" represents a hexahedral element).

	VEM ($k=1$)		VEM ($k=2$)		FEM		S-VEM ($k=2$)	
N	poly	hexa	poly	hexa	Q1	Q2	poly	hexa
4	-1.3676	-1.3783	-1.7005	-1.7081	-1.8115	-1.7332	-1.7001	-1.7079
6	-1.443	-1.4611	-1.7127	-1.7222	-1.7949	-1.7336	-1.7126	-1.7221
8	-1.5025	-1.5122	-1.7276	-1.7293	-1.7745	-1.7334	-1.7275	-1.7293
10	-1.5335	-1.5472	-1.732	-1.7328	-1.7604	-1.7334	-1.7319	-1.7328
16	-1.5983	-1.6084	Failed	-1.7352	-1.7433	-1.7334	-1.7376	-1.7352

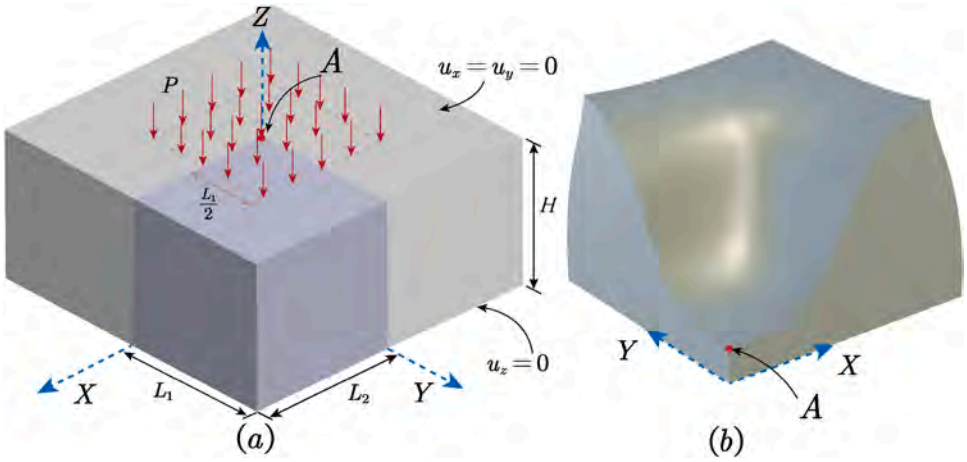

Fig. 11. Block under compression: (a) geometry and boundary conditions, (b) geometry of the 1/4 model after deformation.

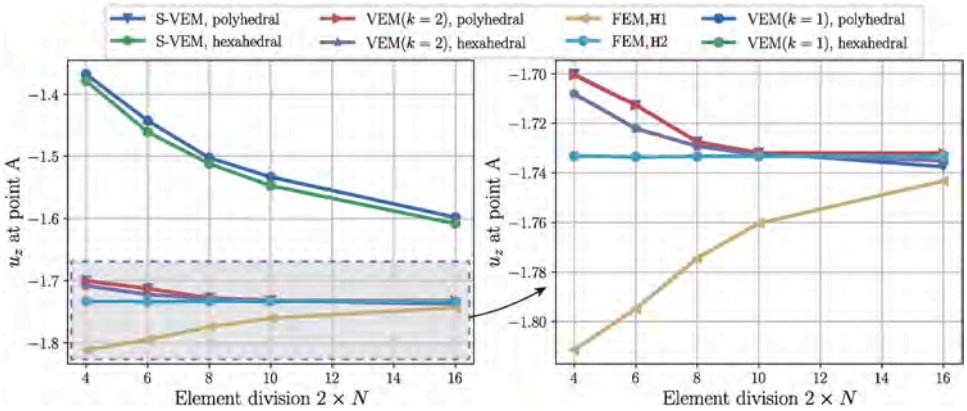

Fig. 12. The vertical displacement u_z of point A obtained by different methods with different discretizations.

The S-VEM can significantly reduce the number of degrees of freedom. The number of degrees of freedom for different elements and different meshe discretizations is listed in Table 2. S-VEM can save 40 % of the number of degrees of freedom when the conventional second-order VEM. Compared with the first-order VEM, the serendipity elements improve the calculation accuracy and reduce the calculation time of the traditional second-order VEM. The contour plots of von-Mises stresses for different meshes obtained by S-VEM without bulk moment are illustrated in Fig. 10.

8.2. Punch problem

The second example is a block under a vertical uniform load P with quasi-static condition. The geometry, dimensions and boundary conditions are illustrated in Fig. 11. Due to symmetry, only 1/4 model is considered. The Neo-Hookean material model with parameter $\lambda = 400.75$ and $\mu = 92.5$ is considered. In addition, the top pressure is selected as $P = 600$.

Similar to the first example, the discretized mesh of different scales is selected with the parameter N. Then the 1/4 block is divided into $2N \times 2N \times 2N$ elements in different directions with $N = 4, 6, 8, 10, 16$. The hexahedral elements and polyhedra elements are used

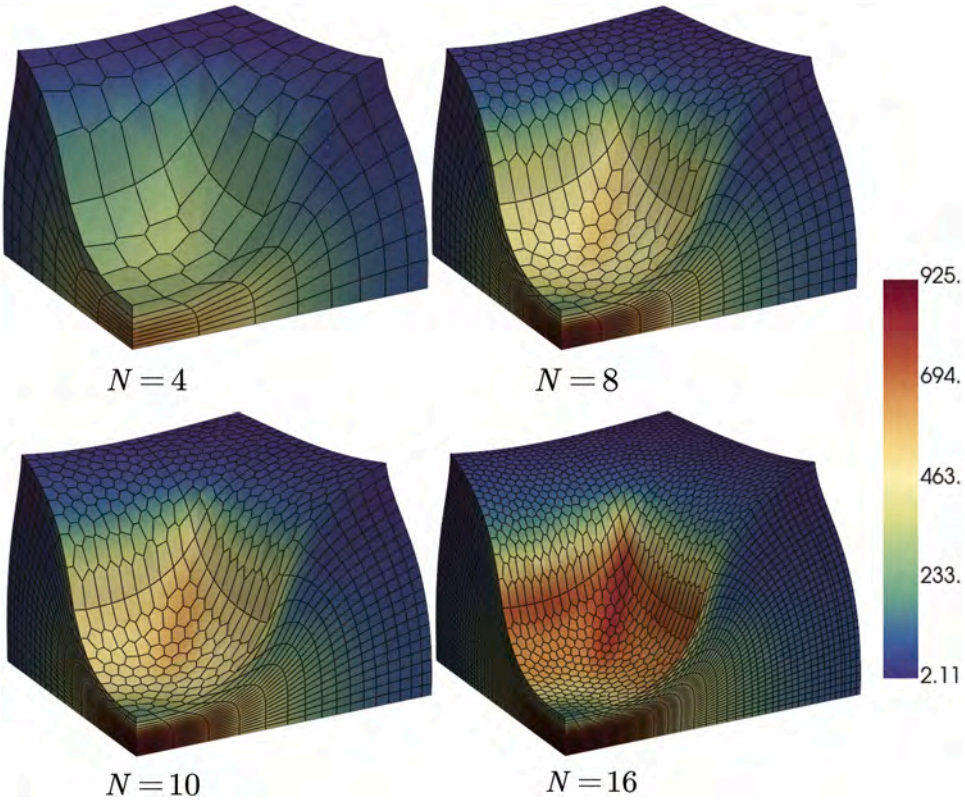

Fig. 13. Contour plots of von-Mises stresses for polyhedral meshes.

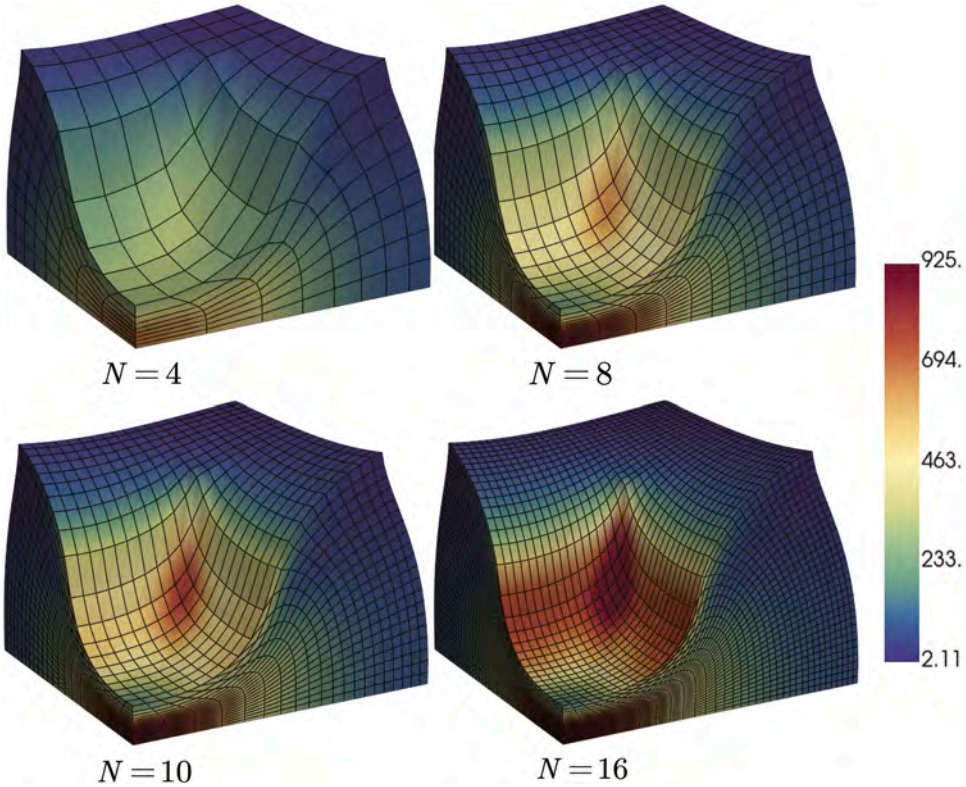

Fig. 14. Contour plots of von-Mises stresses for hexahedral meshes.

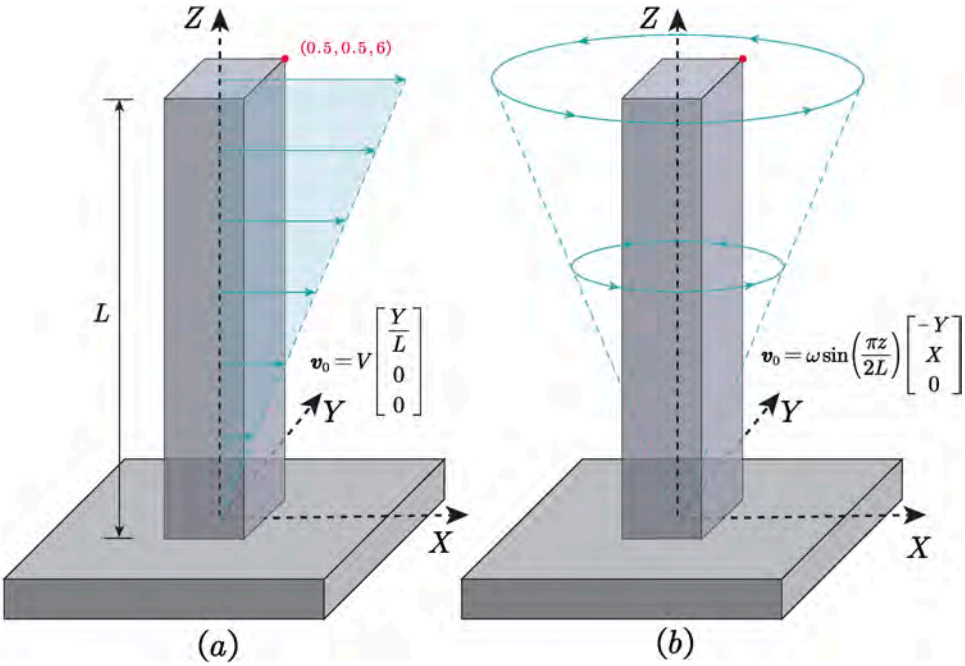

Fig. 15. Column with boundary condition and initial velocity: (a) column under bending, (b) column under twisting.

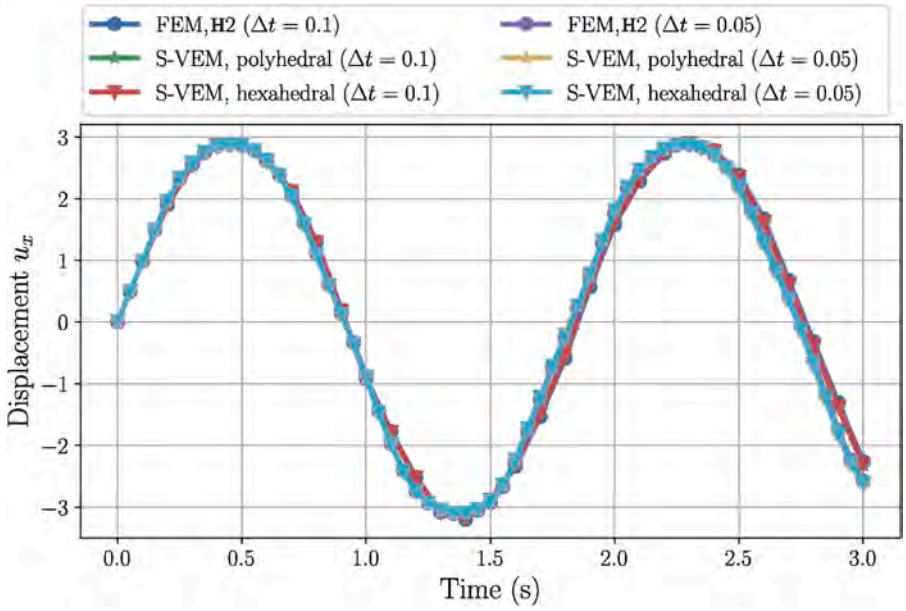

Fig. 16. Time history of u_x at point $(0.5, 0.5, 6)$ obtained by different methods and different time steps.

at the same times. The S-VEM with bulk moment is selected for calculation. For comparison, the FEM (Q1, Q2) and the conventional VEM ($k = 1$, $k = 2$) are used. The geometry of the 1/4 model after deformation is given in Fig. 11. The vertical displacement u_z at point A (see Fig. 11) is selected for convergence analysis in different meshes. The computer used to solve this problem has a memory of 128G (RAM). The results obtained by different methods and different meshes are listed in Table 3 and illustrated in Fig. 12.

For the punch problem, the second-order FEM gives the best results. Even for a coarse mesh ($N = 4$), its accuracy is acceptable. For the first order VEM, the results obtained are often not shown due to poor accuracy. Of course, the first-order VEM can achieve higher accuracy and stability by using a special stabilization, see [11]. At the same time, it should be noted that if the conventional second-order VEM is used, the number of degrees of freedom will be larger, which will lead to huge matrix and in our case causes failure of the simulation for $N = 16$, see Table 3. For S-VEM, the results are very close to those of conventional second-order VEM,

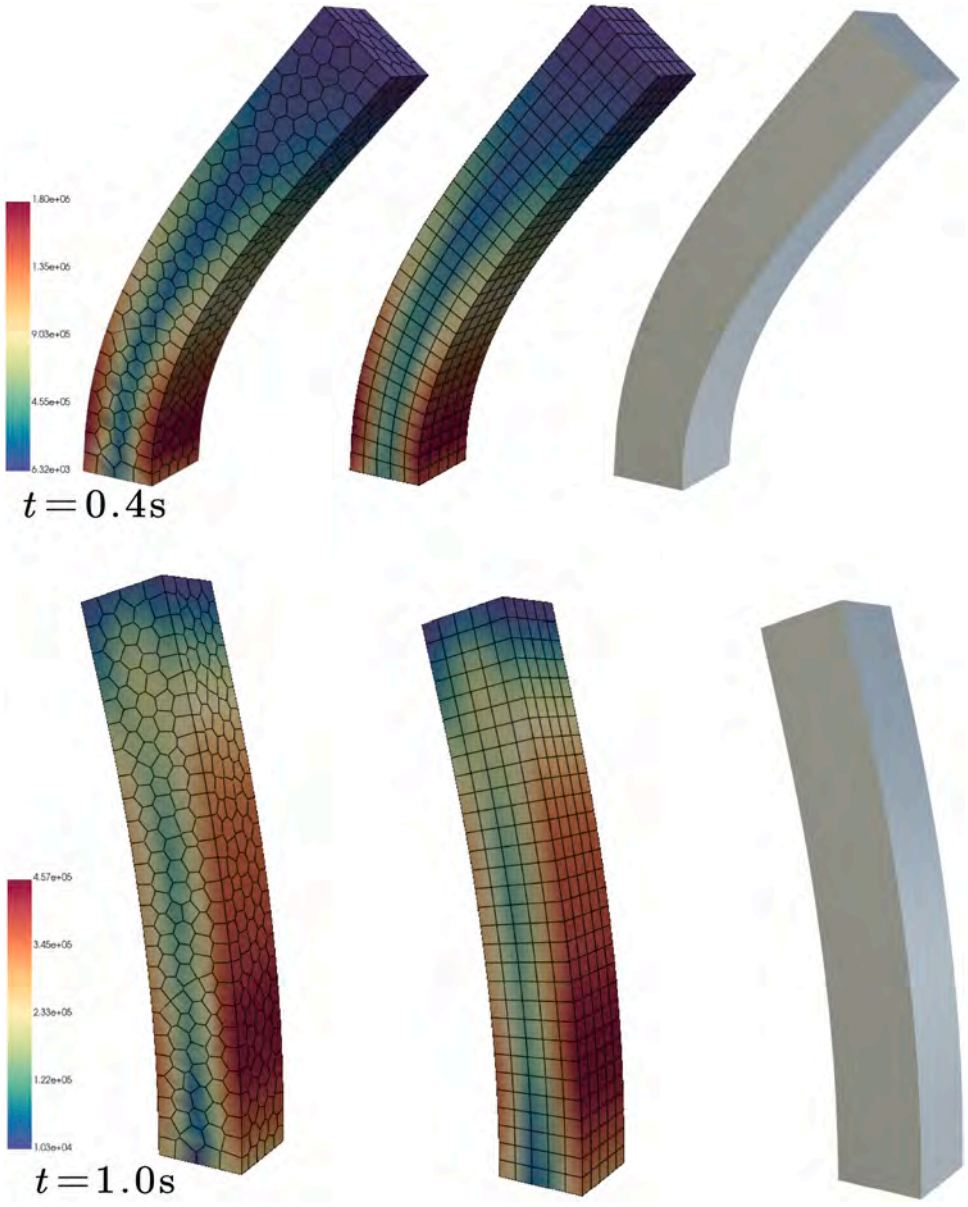

Fig. 17. Contour plot of von-Mises stress obtained by S-VEM with different meshes.

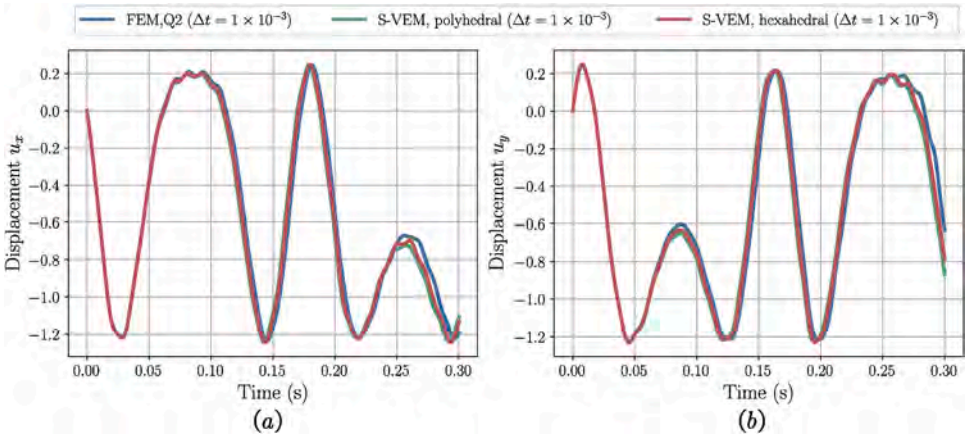

Fig. 18. Time history of u_x and u_y at point $(0.5, 0.5, 6)$ obtained by S-VEM.

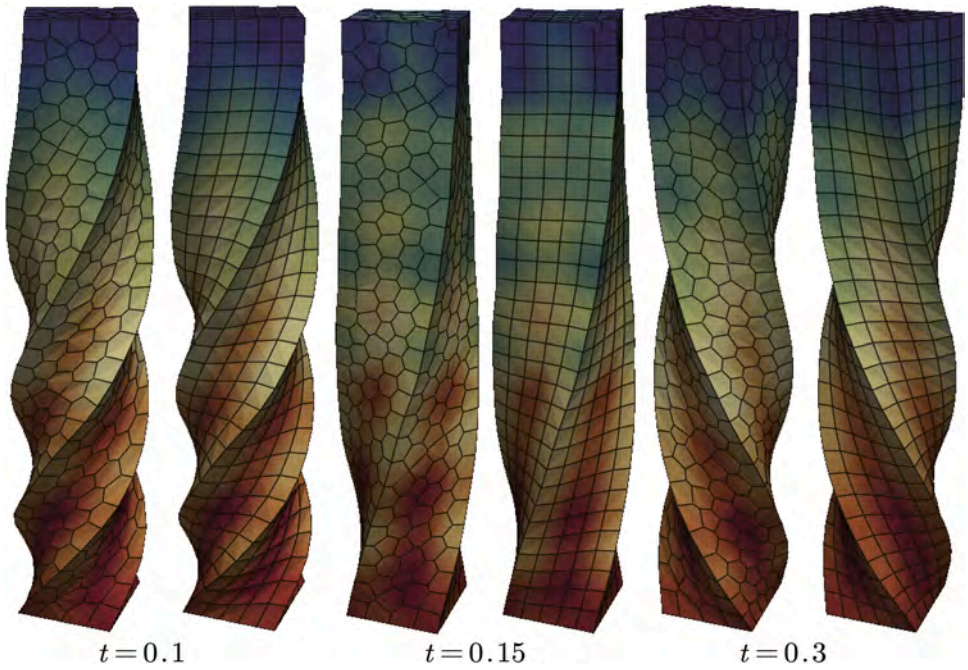

Fig. 19. Contour plot of von-Mises stress obtained by serendipity VEM at different times.

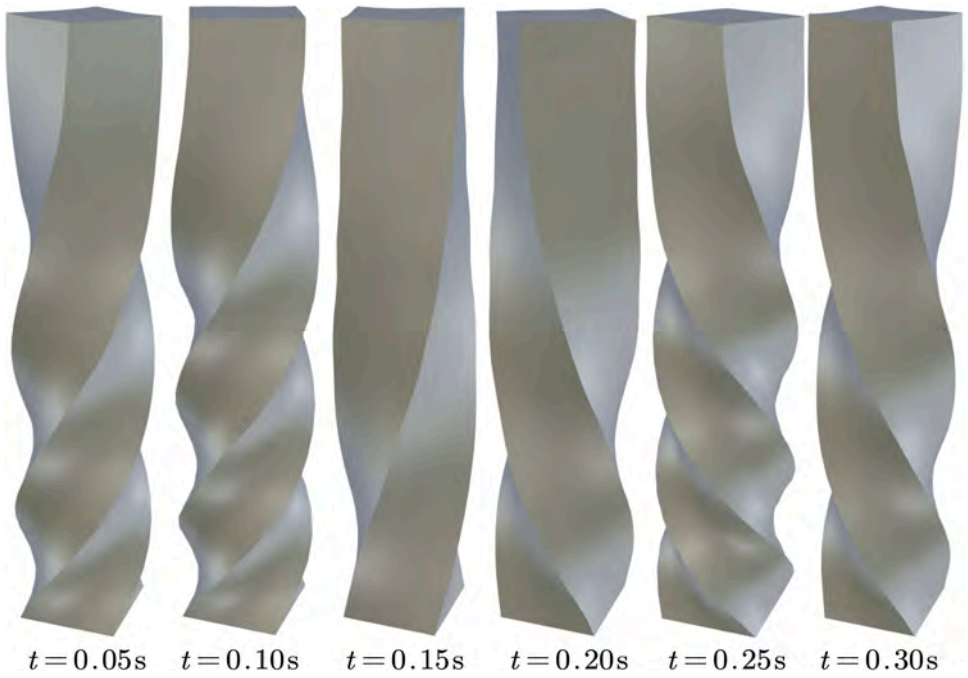

Fig. 20. Deformation along time obtained by serendipity VEM.

while reducing the number of degrees of freedom by about 35 %. It can be seen from this example that S-VEM can reduce matrix size while ensuring computing accuracy.

The contour plots of von-Mises stresses obtained by S-VEM with different meshes are illustrated in Figs. 13 and 14.

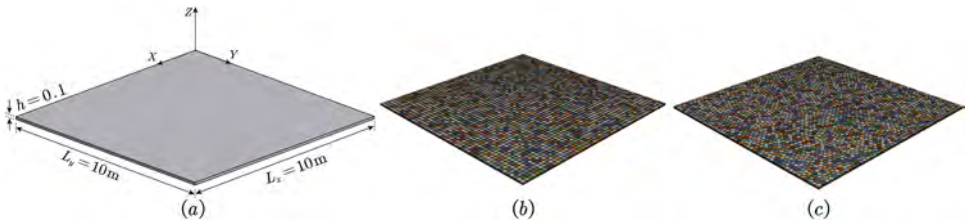

Fig. 21. Thin plate with geometry and VEM meshes: (a) geometry, (b) hexahedral mesh, (c) polyhedral mesh.

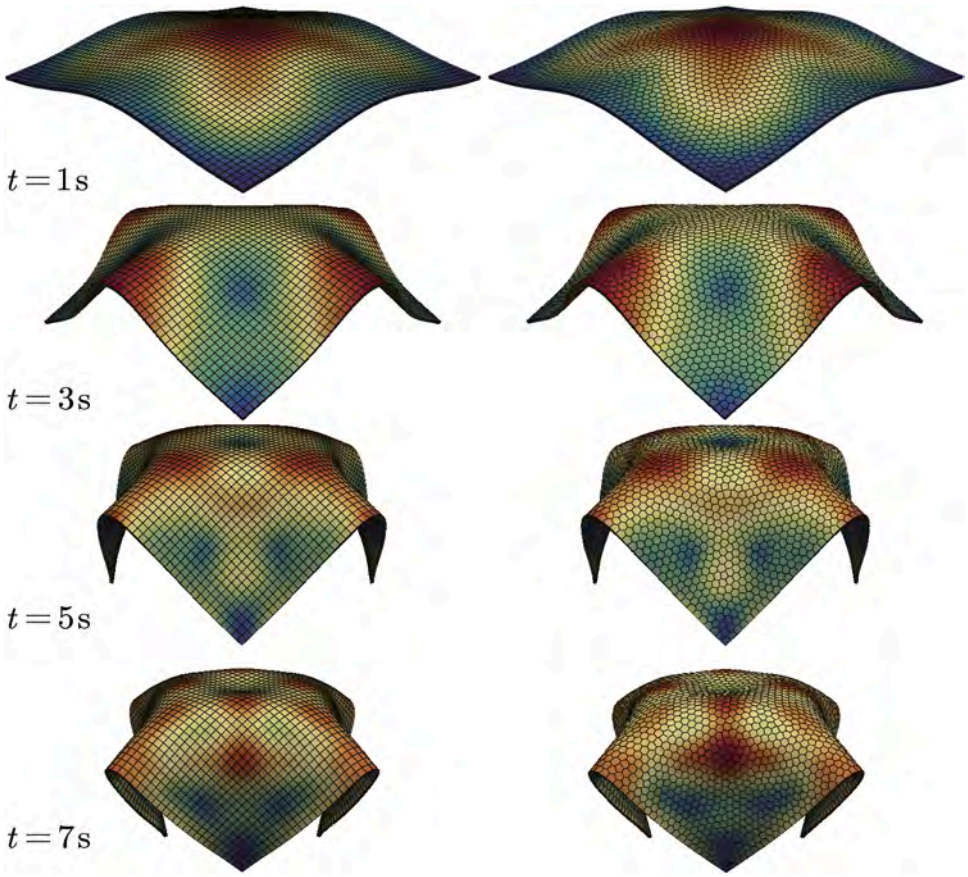

Fig. 22. Contour plot of von-Mises stress obtained by S-VEM at different times.

8.3. Column under bending and twisting

As a finite deformation elastodynamics problem, we consider a three dimensional beam which is fixed at the bottom and free on all other sides. The initial geometry is a parallelepiped of dimension $1 \times 1 \times 6$ as shown in Fig. 15.

Firstly, we consider the column under bending. As shown in Fig. 15(a), the initial velocity field is given as

$$\boldsymbol{v}_0(X, Y, Z) = V \begin{bmatrix} \frac{Y}{L} & 0 & 0 \end{bmatrix}^T, \tag{72}$$

where $V = 10$ m/s and $L = 6$. In addition, stress free conditions and zero displacement initial conditions are applied at the other faces. A Neo-Hookean material model is selected with parameter $E = 1.7 \times 10^7$ Pa, $\nu = 0.3$, and $\rho = 1100$ kg/m^3.

In this example, we use a hexahedral mesh and a polyhedral mesh for the numerical simulations. The time step is selected as $\Delta t = 0.1$ and $\Delta t = 0.05$ for comparison. Here we use only serendipity elements without any additional degrees of freedom (without face moments and volume moments). A FEM solution with hexahedral mesh is used for comparison. For different meshes and different methods, the displacements u_x at point $(0.5, 0.5, 6)$ are illustrated in Fig. 16. It can be seen that the results obtained by VEM compare very well with those obtained by FEM if the same time step is used. In addition, S-VEM with polyhedral meshes yields accurate results. The contour plots of von-Mises stress obtained by VEM with different meshes are given in Fig. 17.

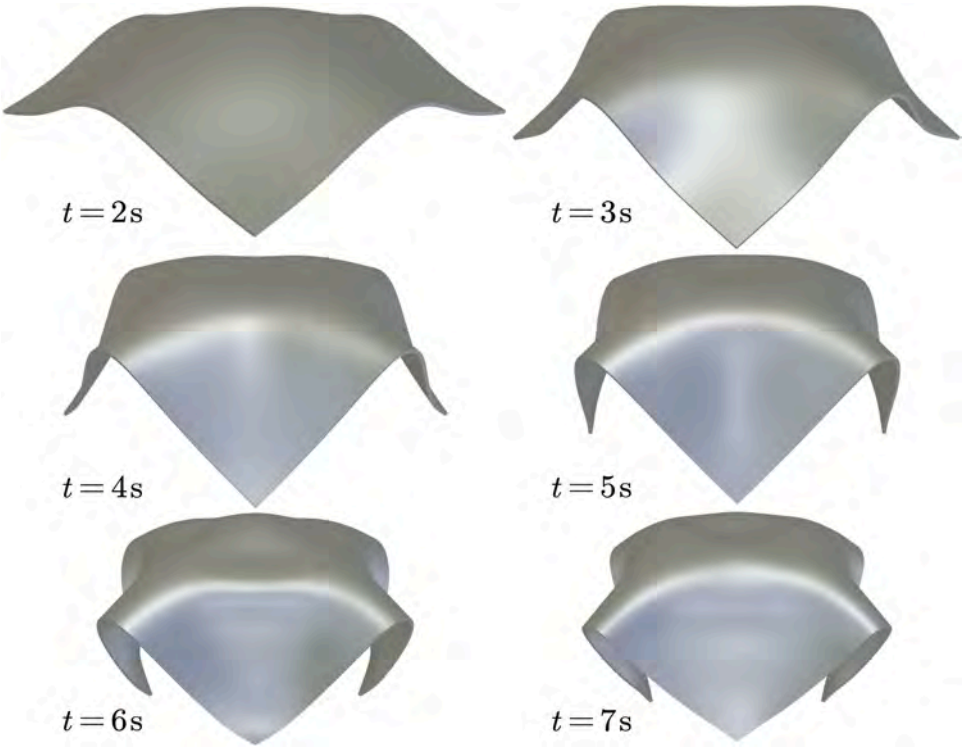

Fig. 23. Deformation along time obtained by S-VEM.

Next, we consider twisting of the column. The test is widely used to test the robustness for extreme nonlinear deformations. As shown in Fig. 15(b), the beam is clamped at the bottom. The initial velocity is assumed as

$$\boldsymbol{v}_0(X,Y,Z) = \Omega \sin\left(\frac{\pi Z}{12}\right)\begin{bmatrix}-Y & X & 0\end{bmatrix}^T \text{ m/s}, \tag{73}$$

where $\Omega = 100$ in this example.

The material parameters are selected as $E = 1.7 \times 10^7$ Pa, $\nu = 0.3$, and $\rho = 1100$ kg/m^3. The time step is chosen as $\Delta t = 0.001$s. Again S-VEM without bulk moment is applied with hexahedral and polyhedral mesh. For different meshes, the displacements u_x and u_y at point $(0.5, 0.5, 6)$ obtained by VEM and FEM are illustrated in Fig. 18. We can clearly appreciate how the VEM solutions for different meshes agree with the solution obtained by FEM. Then, the contour plots of von-Mises stresses obtained by VEM at $t = 0.1$s, $t = 0.15$s, and $t = 0.3$s are shown in Fig. 19. Lastly, the deformation for S-VEM is plotted for different time steps Fig. 20.

8.4. Bending of a thin plate

In this example, we will test the behavior of S-VEM for thin structures. A thin plate with geometry dimension is given in Fig. 21. The initial velocity is given by

$$\boldsymbol{v}_0(X,Y,Z) = \sqrt{\frac{2}{\pi}}\left[\exp\left(-\frac{(X-5)^2}{10}\right) + \exp\left(-\frac{(Y-5)^2}{10}\right)\right]\begin{bmatrix}0\\0\\1\end{bmatrix} \text{ m/s}. \tag{74}$$

In addition, stress free conditions and zero displacement initial conditions are applied for all faces.

A Neo-Hookean material model with parameter $\lambda = 3 \times 10^4$ Pa, $\mu = 2 \times 10^4$, and $\rho = 1000$ kg/m^3 is selected. In Newmark method, the time step is selected as $\Delta t = 0.1$s. The S-VEM without bulk moment is applied with hexahedral and polyhedral mesh. For different meshes, the von-Mises stresses at different times ($t = 1, 3, 5, 7$ s) are illustrated in Fig. 22. Lastly, the deformation obtained by S-VEM is illustrated for the same time steps in Fig. 23.

8.5. Serendipity VEM-FEM hybrid format for soft material

In this example, we will test serendipity VEM-FEM hybrid discretizations for soft material deformation. The geometric model is given in Fig. 7[1]. The Neo-Hookean material model is used with parameters $\lambda = 100$ Pa, $\mu = 40$. Different body forces $\bar{\boldsymbol{f}}$ are given

[1] The geometry can be found at https://github.com/Qinxiaoye/geometry

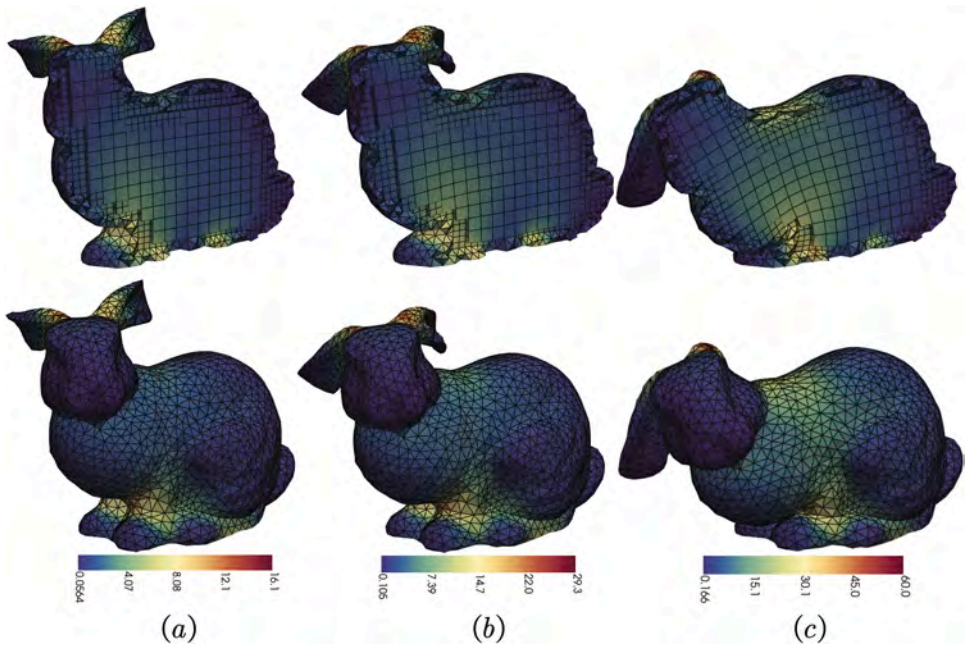

Fig. 24. Von-Mises stresses for different body force $\bar{\boldsymbol{f}}$ obtained by serendipity VEM-FEM hybrid format: (a) $\bar{\boldsymbol{f}} = [0, 0, -50]^T$, (b) $\bar{\boldsymbol{f}} = [0, 0, -100]^T$, (c) $\bar{\boldsymbol{f}} = [0, 0, -200]^T$.

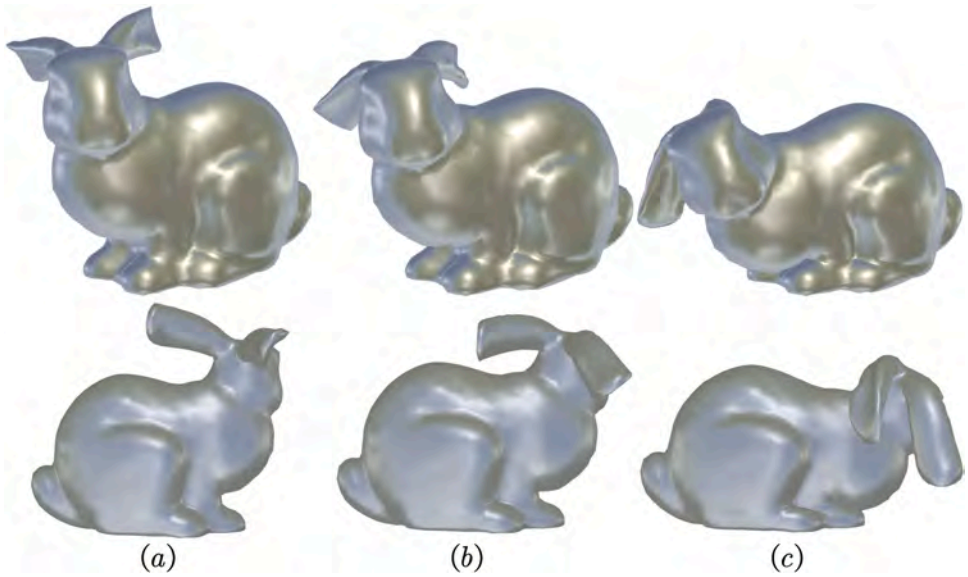

Fig. 25. Deformation for different body force $\bar{\boldsymbol{f}}$ obtained by serendipity VEM-FEM: (a) $\bar{\boldsymbol{f}} = [0, 0, -50]^T$, (b) $\bar{\boldsymbol{f}} = [0, 0, -100]^T$, (c) $\bar{\boldsymbol{f}} = [0, 0, -200]^T$.

for the model as $\bar{\boldsymbol{f}}_z = -50, -100, -200$. The bottom is fixed. As discussed in Section 7, Cartesian hexahedral meshes are used in the model and a triangle discretization is selected for curve surface. Then polygonal elements with hanging nodes are generated. In this example, the FEM is used for cartesian hexahedral elements and the VEM is used for other elements. Since the serendipity virtual element has no additional surface degrees of freedom, it can be directly coupled with the second-order FEM (H2) for solution. For different body forces $\bar{\boldsymbol{f}}$, the von-Mises stresses and deformations are shown in Figs. 24 and 25, respectively.

9. Conclusion

In this work, we developed a novel three-dimensional second-order S-VEM for both static and dynamic analysis of hyperelastic materials. By eliminating the additional moment degrees of freedom which is required in classical second-order VEM formulations,

the proposed serendipity approach significantly reduces the computational complexity while maintaining high accuracy. Moreover, the coupling of S-VEM with second-order serendipity FEM further enhances the applicability of the method for hybrid mesh scenarios. Numerical experiments demonstrate the method's effectiveness and accuracy in capturing nonlinear hyperelastic behavior under large deformations and dynamic loading. This work represents the first application of three-dimensional S-VEM to nonlinear elasticity problems and opens new avenues for efficient and flexible computational modeling of advanced materials. Future work will focus on extending the method to nearly incompressible materials, and more complex multi-physical coupling problems and exploring adaptive strategies for further computational efficiency.

CRediT authorship contribution statement

Bing-Bing Xu: Writing – original draft, Visualization, Software, Data curation; **Lourenco Beirao da Veiga:** Writing – original draft; **Yongjie Jessica Zhang:** Writing – review & editing; **Peter Wriggers:** Writing – review & editing, Supervision.

Data availability

No data was used for the research described in the article.

Declaration of competing interest

The authors declare that they have no known competing financial interests or personal relationships that could have appeared to influence the work reported in this paper.

References

[1] T. Belytschko, W.K. Liu, B. Moran, K. Elkhodary, Nonlinear Finite Elements for Continua and Structures, John wiley & sons, 2014.
[2] P. Wriggers, Nonlinear Finite Element Methods, Springer Verlag, 2008. https://doi.org/10.1007/978-3-642-56865-7
[3] I. Castañar, J. Baiges, R. Codina, A stabilized mixed finite element approximation for incompressible finite strain solid dynamics using a total lagrangian formulation, Comput. Methods Appl. Mech. Eng. 368 (2020) 113164. https://doi.org/10.1016/j.cma.2020.113164
[4] S. Zhang, S.D.N. Lourenço, D. Wu, C. Zhang, X. Hu, Essentially non-hourglass SPH elastic dynamics, J. Comput. Phys. 510 (2024) 113072. https://doi.org/10.1016/j.jcp.2024.113072
[5] D. Wu, X. Tang, S. Zhang, X. Hu, Unified non-hourglass formulation for total lagrangian SPH solid dynamics, Comput. Mech. (2024) 1–33. https://doi.org/10.1007/s00466-024-02552-7
[6] S. Zhang, D. Wu, S.D.N. Lourenço, X. Hu, A generalized non-hourglass updated lagrangian formulation for SPH solid dynamics, Comput. Methods Appl. Mech. Eng. 440 (2025) 117948. https://doi.org/10.1016/j.cma.2025.117948
[7] X. Du, G. Zhao, W. Wang, H. Fang, Nitsche's method for non-conforming multipatch coupling in hyperelastic isogeometric analysis, Comput. Mech. 65 (3) (2019) 687–710. https://doi.org/10.1007/s00466-019-01789-x
[8] L. Beirao da Veiga, F. Brezzi, A. Cangiani, G. Manzini, L. Marini, A. Russo, Basic principles of virtual element methods, Math. Models Methods Appl. Sci. 23 (2012) 199–214. https://doi.org/10.1142/S0218202512500492
[9] L. Beirao da Veiga, Brezzi, Franco, Marini, Luisa Donatella, Russo, Alessandro, Mixed virtual element methods for general second order elliptic problems on polygonal meshes, ESAIM Math. Modell. Numer. Anal. 26 (2014) 727–747. https://doi.org/10.1051/m2an/2015067
[10] H. Chi, G. Paulino, Some basic formulations of the virtual element method (VEM) for finite deformations, Comput. Methods Appl. Mech. Eng. 318 (2016) 995–1023. https://doi.org/10.1016/j.cma.2016.12.020
[11] P. Wriggers, B. Reddy, W. Rust, B. Hudobivnik, Efficient virtual element formulations for compressible and incompressible finite deformations, Comput. Mech. 60 (2017) 995–1023. https://doi.org/10.1007/s00466-017-1405-4
[12] D. van Huyssteen, B.D. Reddy, A virtual element method for isotropic hyperelasticity, Comput. Methods Appl. Mech. Eng. 367 (2020) 113134. https://doi.org/10.1016/j.cma.2020.113134
[13] M.L. de Bellis, P. Wriggers, B. Hudobivnik, Serendipity virtual element formulation for nonlinear elasticity, Comput. Struct. 223 (2019) 106094. https://doi.org/10.1016/j.compstruc.2019.07.003
[14] P. Wriggers, W. Rust, B. Reddy, A virtual element method for contact, Comput. Mech. 58 (2016) 995–1023. https://doi.org/10.1007/s00466-016-1331-x
[15] F. Aldakheel, B. Hudobivnik, E. Artioli, L. Beirao da Veiga, P. Wriggers, Curvilinear virtual elements for contact mechanics, Comput. Methods Appl. Mech. Eng. 372 (2020) 113394. https://doi.org/10.1016/j.cma.2020.113394
[16] W. Shen, M. Ohsaki, J. Zhang, A 2-dimentional contact analysis using second-order virtual element method, Comput. Mech. 70 (2022) 995–1023. https://doi.org/10.1007/s00466-022-02165-y
[17] M. Cihan, B. Hudobivnik, J. Korelc, P. Wriggers, A virtual element method for 3D contact problems with non-conforming meshes, Comput. Methods Appl. Mech. Eng. 402 (2022) 115385. https://doi.org/10.1016/j.cma.2022.115385
[18] F. Aldakheel, B. Hudobivnik, A. Hussein, P. Wriggers, Phase-field modeling of brittle fracture using an efficient virtual element scheme, Comput. Methods Appl. Mech. Eng. 341 (2018) 443–466. https://doi.org/10.1016/j.cma.2018.07.008
[19] T.-R. Liu, F. Aldakheel, M.H. Aliabadi, Virtual element method for phase field modeling of dynamic fracture, Comput. Methods Appl. Mech. Eng. 411 (2023) 116050. https://doi.org/10.1016/j.cma.2023.116050
[20] F. Aldakheel, B. Hudobivnik, P. Wriggers, Virtual element formulation for phase-field modeling of ductile fracture, Int. J. Multiscale Comput. Eng. 17 (2019) 181–200. https://doi.org/10.1615/IntJMultCompEng.2018026804
[21] P. Wriggers, B. Hudobivnik, A low order virtual element formulation for finite elasto-plastic deformations, Comput. Methods Appl. Mech. Eng. 327 (2017) 4702–4725. https://doi.org/10.1016/j.cma.2017.08.053
[22] B. Hudobivnik, F. Aldakheel, P. Wriggers, A low order 3D virtual element formulation for finite elasto-plastic deformations, Comput. Mech. 63 (2019) 4702–4725. https://doi.org/10.1007/s00466-018-1593-6
[23] M. Cihan, B. Hudobivnik, F. Aldakheel, P. Wriggers, 3D mixed virtual element formulation for dynamic elasto-plastic analysis, Comput. Mech. 68 (2021) 1–18. https://doi.org/10.1007/s00466-021-02010-8
[24] K. Park, H. Chi, G. Paulino, On nonconvex meshes for elastodynamics using virtual element methods with explicit time integration, Comput. Methods Appl. Mech. Eng. 356 (2019) 669–684. https://doi.org/10.1016/j.cma.2019.06.031
[25] K. Park, H. Chi, G. Paulino, Numerical recipes for elastodynamic virtual element methods with explicit time integration, Int. J. Numer. Methods Eng. 121 (2019) 1–31. https://doi.org/10.1002/nme.6173
[26] M. Cihan, B. Hudobivnik, F. Aldakheel, P. Wriggers, Virtual element formulation for finite strain elastodynamics, Comput. Model. Eng. Sci. 129 (2021) 1151–1180. https://doi.org/10.32604/cmes.2021.016851

[27] N. Sukumar, M. Tupek, Virtual elements on agglomerated finite elements to increase the critical time step in elastodynamic simulations, Int. J. Numer. Methods Eng. 123 (2022) 4702–4725. https://doi.org/10.1002/nme.7052
[28] L. Beirao da Veiga, F. Brezzi, L.D. Marini, A. Russo, The Hitchhiker's guide to the virtual element method, Math. Models Methods Appl. Sci. 24 (08) (2014) 1541–1573. https://doi.org/10.1142/S021820251440003X
[29] O. Sutton, The virtual element method in 50 lines of MATLAB, Numer. Algo. 75 (2017). https://doi.org/10.1007/s11075-016-0235-3
[30] M. Mengolini, M. Benedetto, A. Aragón, An engineering perspective to the virtual element method and its interplay with the standard finite element method, Comput. Methods Appl. Mech. Eng. 350 (2019) 995–1023. https://doi.org/10.1016/j.cma.2019.02.043
[31] L. Beirao da Veiga, F. Dassi, A. Russo, High-order virtual element method on polyhedral meshes, Comput. Math. Appl. 74 (5) (2017) 1110–1122. https://doi.org/10.1016/j.camwa.2017.03.021
[32] F. Dassi, L. Mascotto, Exploring high-order three dimensional virtual elements: bases and stabilizations, Comput. Math. Appl. 75 (9) (2018) 3379–3401. https://doi.org/10.1016/j.camwa.2018.02.005
[33] J. Huang, Y. Yu, Some estimates for virtual element methods in three dimensions, Comput. Methods Appl. Math. 23 (2022). https://doi.org/10.1515/cmam-2022-0062
[34] M. Visinoni, A family of three-dimensional virtual elements for Hellinger-Reissner elasticity problems, Comput. Math. Appl. 155 (2024) 97–109. https://doi.org/10.1016/j.camwa.2023.11.034
[35] B.-B. Xu, W.-L. Fan, P. Wriggers, High-order 3D virtual element method for linear and nonlinear elasticity, Comput. Methods Appl. Mech. Eng. 431 (2024) 117258. https://doi.org/10.1016/j.cma.2024.117258
[36] L. Beirao da Veiga, F. Brezzi, L.D. Marini, A. Russo, Serendipity nodal VEM spaces, Comput. Fluids 141 (2016) 2–12. Advances in Fluid-Structure Interaction. https://doi.org/10.1016/j.compfluid.2016.02.015
[37] L. Beirao da Veiga, F. Brezzi, F. Dassi, L. Marini, A. Russo, Serendipity virtual elements for general elliptic equations in three dimensions, Chin. Ann. Math. Ser. B 39 (2018) 315–334. https://doi.org/10.1007/s11401-018-1066-4
[38] L. Beirao da Veiga, F. Brezzi, F. Dassi, L.D. Marini, A. Russo, Virtual element approximation of 2D magnetostatic problems, Comput. Methods Appl. Mech. Eng. 327 (2017) 173–195. Advances in Computational Mechanics and Scientific Computation-the Cutting Edge. https://doi.org/10.1016/j.cma.2017.08.013
[39] J. Korelc, P. Wriggers, Automation of Finite Element Methods, Springer, 2016.
[40] L. Beirao da Veiga, F. Brezzi, L.D. Marini, A. Russo, The virtual element method, Acta Numer. 32 (2023) 123–202. https://doi.org/10.1017/s0962492922000095
[41] Y.J. Zhang, Geometric Modeling and Mesh Generation from Scanned Images, Chapman and Hall, 2016. https://doi.org/10.1201/9781315372259
[42] J. Qian, Y. Zhang, Automatic unstructured all-hexahedral mesh generation from B-Reps for non-manifold CAD assemblies, Eng. Comput. 28 (4) (2011) 345–359. https://doi.org/10.1007/s00366-011-0232-z
[43] H. Tong, E. Halilaj, Y.J. Zhang, Hybridoctree hex: hybrid octree-based adaptive all-hexahedral mesh generation with jacobian control, J. Comput. Sci. 78 (2024) 102278. https://doi.org/10.1016/j.jocs.2024.102278
[44] H.-Y. Kim, H.-G. Kim, Efficient isoparametric trimmed-hexahedral elements with explicit shape functions, Comput. Methods Appl. Mech. Eng. 372 (2020) 113316. https://doi.org/10.1016/j.cma.2020.113316
[45] H.-Y. Kim, H.-G. Kim, A hexahedral-dominant FE meshing technique using trimmed hexahedral elements preserving sharp edges and corners, Eng. Comput. 38 (5) (2021) 4307–4322. https://doi.org/10.1007/s00366-021-01526-0
[46] A. Abdelkader, C.L. Bajaj, M.S. Ebeida, A.H. Mahmoud, S.A. Mitchell, J.D. Owens, A.A. Rushdi, Vorocrust: voronoi meshing without clipping, ACM Trans. Graph. 39 (3) (2020). https://doi.org/10.1145/3337680